Nanopore direct RNA sequencing maps an Arabidopsis N6 methyladenosine epitranscriptome

Matthew T. Parker[1†], Katarzyna Knop[1†], Anna V. Sherwood[1†], Nicholas J. Schurch[1†‡], Katarzyna Mackinnon[1], Peter D. Gould[2], Anthony Hall[3], Geoffrey J. Barton[1*] and Gordon G. Simpson[1,4*]

[1]School of Life Sciences, University of Dundee, Dow Street, Dundee DD1 5EH, UK

[2]Institute of Integrative Biology, University of Liverpool, Crown Street, Liverpool, L69 7ZB, UK

[3]Earlham Institute, Norwich Research Park, Norwich, NR4 7UZ, UK

[4]James Hutton Institute, Invergowrie, DD2 5DA, UK

[†]Contributed equally

*Correspondence: g.g.simpson@dundee.ac.uk ; g.j.barton@dundee.ac.uk

Current Address:

[‡]Biomathematics and Statistics Scotland, The James Hutton Institute, Aberdeen, AB15 8QH, UK

Abstract

Understanding genome organization and gene regulation requires insight into RNA transcription, processing and modification. We adapted nanopore direct RNA sequencing to examine RNA from a wild-type accession of the model plant *Arabidopsis thaliana* and a mutant defective in mRNA methylation (m^6A). Here we show that m^6A can be mapped in full-length mRNAs transcriptome-wide and reveal the combinatorial diversity of cap-associated transcription start sites, splicing events, poly(A) site choice and poly(A) tail length. Loss of m^6A from 3′ untranslated regions is associated with decreased relative transcript abundance and defective RNA 3′ end formation. A functional consequence of disrupted m^6A is a lengthening of the circadian period. We conclude that nanopore direct RNA sequencing can reveal the complexity of mRNA processing and modification in full-length single molecule reads. These findings can refine Arabidopsis genome annotation. Further, applying this approach to less well-studied species could transform our understanding of what their genomes encode.

Introduction

Patterns of pre-mRNA processing and base modifications determine eukaryotic mRNA coding potential and fate. Alternative transcripts produced from the same gene can differ in the position of the start site, the site of cleavage and polyadenylation, and the combination of exons spliced into the mature mRNA. Collectively termed the epitranscriptome, RNA modifications play crucial context-specific roles in gene expression[1,2]. The most abundant internal modification of mRNA is methylation of adenosine at the N6 position (m^6A). Knowledge of RNA modifications and processing combinations is essential to understand gene expression and what genomes really encode.

RNA sequencing (RNAseq) is used to dissect transcriptome complexity: it involves copying RNA into complementary DNA (cDNA) with reverse transcriptases (RTs) and then sequencing the subsequent DNA copies. RNAseq reveals diverse features of transcriptomes, but limitations can include

misidentification of 3′ ends through internal priming[3], spurious antisense and splicing events produced by RT template switching[4,5], and the inability to detect all base modifications in the copying process[6]. The fragmentation of RNA prior to short-read sequencing makes it difficult to interpret the combination of authentic RNA processing events and remains an unsolved problem[7].

We investigated whether long-read direct RNA sequencing (DRS) with nanopores[8] could reveal the complexity of Arabidopsis mRNA processing and modifications. In nanopore DRS, the protein pore (nanopore) sits in a membrane through which an electrical current is passed, and intact RNA is fed through the nanopore by a motor protein[8]. Each RNA sequence within the nanopore (5 bases) can be identified by the magnitude of signal it produces. Arabidopsis is a pathfinder model in plant biology, and its genome annotation strongly influences the annotation and our understanding of what other plant genomes encode. We applied nanopore DRS and Illumina RNAseq to wild-type Arabidopsis (Col-0) and mutants defective in m^{6}A[9] and exosome-mediated RNA decay[10]. We reveal m^{6}A and combinations of RNA processing events (alternative patterns of 5′ capped transcription start sites, splicing, 3′ polyadenylation and poly(A) tail length) in full-length Arabidopsis mRNAs transcriptome-wide.

Results

Nanopore DRS detects long, complex mRNAs and short, structured non-coding RNAs

We purified poly (A)+ RNA from four biological replicates of 14-day-old Arabidopsis Col-0 seedlings. We incorporated synthetic External RNA Controls Consortium (ERCC) RNA Spike-In mixes into all replicates[11,12] and carried out nanopore DRS. Illumina RNAseq was performed in parallel on similar material. Using Guppy base-calling (Oxford Nanopore Technologies) and minimap2 alignment software[13], we identified around 1 million reads per sample (Supplementary table 1). The longest read alignments were 12.7 kb for mRNA transcribed from AT1G48090, spanning 63 exons, (Figure 1A), and 12.8 kb for mRNA transcribed from At1G67120, spanning 58 exons (Supplementary

figure 1A). These represent some of the longest contiguous mRNAs sequenced from Arabidopsis. Among the shortest read alignments were those spanning genes encoding highly structured non-coding RNAs such as UsnRNAs and snoRNAs such as U3 (Figure 1B).

Base-calling errors in nanopore DRS are non-random

We used ERCC RNA Spike-Ins[11] as internal controls to monitor the properties of the sequencing reads. The spike-ins were detected in a quantitative manner (Supplementary figure 1B), consistent with the suggestion that nanopore sequencing is quantitative[8]. For the portion of reads that align to the reference, sequence identity was 92% when measured against the ERCC RNA spike-ins (Supplementary figure 1C). The errors showed evidence of base specificity (Supplementary figure 1D, E). For example, guanine was under-represented and uracil over-represented in indels and substitutions relative to the reference nucleotide (nt) distribution. In some situations, this bias could impact the utility of interpreting nanopore sequence errors. We used the proovread software tool[14] and parallel Illumina RNAseq data to correct base-calling errors in the nanopore reads[15].

Artefactual splitting of raw signal affects transcript interpretation

We detected artefacts caused by the MinKNOW software splitting raw signal from single molecules into two or more reads. As a result, alignments comprising apparently novel 3′ ends were mapped as adjacent to alignments with apparently novel 5′ ends (Supplementary figure 1F). A related phenomenon called over-splitting was recently reported in nanopore DNA sequencing[16]. Over-splitting can be detected when two reads sequenced consecutively through the same pore are mapped to adjacent loci in the genome[16]. Over-splitting in nanopore DRS generally occurs at low frequency (< 2% of reads). However, RNAs originating from specific gene loci, such as *RH3* (*AT5G26742*), appear to be more susceptible, with up to 20% of reads affected across multiple sequencing experiments (Supplementary figure 1F).

Spurious antisense reads are rare or absent in nanopore DRS

Since only two out of 9,445 (0.02%) reads mapped antisense to the ERCC RNA Spike-In collection[11] and 0 of 19,665 reads mapped antisense to the highly expressed gene *RUBISCO ACTIVASE* (*RCA*) (*AT2G39730*), we conclude that spurious antisense is rare or absent from nanopore DRS data. This simplifies the interpretation of authentic antisense RNAs, which is important in Arabidopsis because the distinction between RT-dependent template switching and authentic antisense RNAs produced by RNA-dependent RNA polymerases that copy mRNA is not straightforward[17]. For example, by nanopore DRS, we could identify Arabidopsis long non-coding antisense RNAs, such as those at the auxin efflux carriers *PIN4* and *PIN7* (Figure 1C, Supplementary figure 1G). The existence of these previously unannotated antisense RNAs was supported by Illumina RNAseq of wild-type Col-0 and the exosome mutant *hen2–2* (Figure 1C, Supplementary figure 1G), the latter of which had a 13-fold increase in abundance of these antisense RNAs. Consequently, the low level of steady-state accumulation of some antisense RNAs may explain why they are currently unannotated.

Nanopore DRS confirms sites of RNA 3′ end formation and estimates poly(A) tail length

Ligation of the motor protein adapter to RNA 3′ ends results in nanopores sequencing mRNA poly(A) tails first. We used the nanopolish-polyA software tool to estimate poly(A) tail lengths for individual transcripts[18]. This approach indicated an average length of 76 nt for Arabidopsis mRNA poly(A) tails, but with a wide range in estimated lengths for individual mRNAs (95% were in the 13–197 nt range; Figure 2A). The generally shorter poly(A) tails of chloroplast- and mitochondria-encoded transcripts, which are a feature of RNA decay in these organelles, were also detectable. We found that poly(A) tail length correlates negatively with gene expression in Arabidopsis (Spearman's $\rho=-0.3$, $p=2\times10^{-133}$, 95% CIs [−0.32, −0.28]; Supplementary figure 2A), consistent with other species analysed by short-read TAILseq[19].

We previously mapped Arabidopsis mRNA 3′ ends transcriptome-wide using Helicos sequencing[20]. We compared the position of 3′ ends of nanopore DRS read alignments and Helicos data genome-wide. The median genomic distance between nanopore DRS and Helicos 3′ ends was 0 ± 13 nt (one standard deviation) demonstrating close agreement between these orthogonal technologies (Figure 2B). Likewise, the overall distribution of the 3′ ends of aligned nanopore DRS reads resembles the pattern we previously reported with Helicos data[20]. For example, 97% of nanopore DRS 3′ ends (4,152,800 reads at 639,178 unique sites, 93% of all unique sites) mapped to either annotated 3′ untranslated regions (UTRs) or downstream of the current annotation. Mapping of 3′ ends to coding sequences or 5′UTRs was rare (2.8%, 119,524 reads at 39,610 unique sites, 5.8% of all unique sites), and mapping to introns even rarer (0.29%, 12,554 reads at 7,791 unique sites, 1.1% of unique sites). Even so, examples of the latter included sites of alternative polyadenylation with well-established regulatory roles, such as in mRNA encoding the RNA-binding protein FPA, which controls flowering time[21] (Figure 2C), and in mRNA encoding the histone H3K9 demethylase IBM1, which controls levels of genic DNA methylation[22] (Supplementary figure 2B).

Since RT-dependent internal priming can result in the misinterpretation of authentic cleavage and polyadenylation sites[3], we next determined whether nanopore DRS was compromised in this way. To address this issue, we examined whether the 3′ ends of nanopore DRS reads mapped to potential internal priming substrates comprised of six consecutive adenosines within a transcribed coding sequence (according to the Arabidopsis Information Portal Col-0 genome annotation, Araport11). Of the 10,116 such oligo $(A)_6$ sequences, only four have read alignments terminating within 13 nt in all four datasets. Of these, two were not detectable after error correction with proovread (suggesting that they resulted from alignment errors) and the other two mapped to the terminal exon of coding sequence annotation, indicating that they may be authentic 3′ ends. Hence, internal priming is rare or absent in nanopore DRS data. Overall, we conclude that nanopore DRS can identify multiple authentic features of RNA 3′ end processing.

Cap-dependent 5′ RNA detection by nanopore DRS

Nanopore DRS reads are frequently truncated prior to annotated transcription start sites, resulting in a 3′ bias of genomic alignments (Figure 3A)[15]. Consequently, it is impossible to determine which, if any, aligned reads correspond to full-length transcripts. To address this issue, we used cap-dependent ligation of a biotinylated 5′ adapter RNA to purify capped mRNAs. We then re-sequenced two biological replicates of Arabidopsis Col-0 incorporating 5′ adapter ligation (Supplementary table 1) and filtered the reads for 5′ adapter RNA sequences using the sequence alignment tool BLASTN and specific criteria (Supplementary table 2). We then used high confidence examples of sequences that passed or failed these criteria to train a convolutional neural network to detect the 5′ adapter RNA in the raw signal (Supplementary figure 3A–C). Hence, we improved 5′ adapter-ligated RNA detection without requiring base-calling or genome alignment, and demonstrated enrichment of full-length, cap-dependent mRNA sequences (Figure 3A, B). This procedure reduced the median 3′ bias of nanopore read alignments per gene (as measured by quartile coefficient of variation of per base coverage) from 0.45 (95% CIs [0.43,0.47]) to 0.08 (95% CIs [0.07,0.09]; Figure 3B).

In order to determine whether the 5′ ends we detected reflect full-length mRNAs, we compared them against annotated transcription start sites in datasets derived from full-length Arabidopsis cDNA clones[23]. We found that 41% of adapter-ligated nanopore DRS reads mapped within 5 nt of transcription start sites and 60% mapped within 13 nt (Figure 3C). We also detected recently defined examples of alternative 5′ transcription start sites[24] at specific Arabidopsis genes (Supplementary figure 3D). We therefore conclude that this approach is effective in detecting authentic mRNA 5′ ends.

Reads with adapters had, on average, 11 nt more at their 5′ ends that could be aligned to the genome compared with the most common 5′ alignment position of reads lacking the 5′ adapter

RNA (Figure 3D). This difference may be explained by loss of processive control by the motor protein when the end of an RNA molecule enters the pore. As a result, the 5′ end of RNA is not correctly sequenced. Consistent with these Arabidopsis transcriptome-wide nanopore DRS data, reads mapping to the synthetic ERCC RNA Spike-Ins and *in vitro* transcribed RNAs also lacked ~11 nt of authentic 5′ sequence (Supplementary figure 3E, F). However, the precise length of 5′ sequence missing from all of these RNAs varied, suggesting that sequence- or context-specific effects on sequence accuracy are associated with the passage of 5′ RNA through the pore (Figure 3D, Supplementary figure 3E, F).

Despite the close agreement between nanopore DRS, Illumina RNAseq and full-length cDNA data[23] at *RCA*, the start site annotated in Araport11 and the *Arabidopsis thaliana* Reference Transcript Dataset 2 (AtRTD2)[25] is quite different (Figure 3E). The apparent overestimation of 5′UTR length is widespread in Araport11 annotation (Supplementary figure 3G), consistent with the assessment of capped Arabidopsis 5′ ends detected by nanoPARE sequencing[26]. Consequently, with appropriate modification to the current protocol, such as we describe here, nanopore DRS data can be used to revise Arabidopsis transcription start site annotations.

Nanopore DRS reveals the complexity of splicing events

In single reads, nanopore sequencing revealed some of the most complex splicing combinations so far identified in the Arabidopsis transcriptome. For example, the splicing pattern of a 12.7 kb read alignment, comprised of 63 exons, agreed exactly with the *AT1G48090.4* isoform annotated in Araport11 (Figure 1A). Mutually exclusive alternative splicing of *FLM (AT1G77080*) exons that mediate the thermosensitive response controlling flowering time[27] was also detected (Figure 4A). However, a combination of base-calling and alignment errors contributed to the misidentification of splicing events for uncorrected DRS data: 58% (170,702) of the unique splice junctions detected in the combined set of replicate data were absent from Araport11 and AtRTD2 annotations and were

196 unsupported by Illumina RNAseq (Figure 4B, Supplementary table 3). We applied proovread[14,15]
197 error correction with the parallel Illumina RNAseq data and then re-analysed the corrected and
198 uncorrected nanopore DRS data. After error correction, only 13% (39,061) of unique splice junctions
199 were unsupported by an orthogonal dataset, consistent with an improvement in alignment accuracy.
200 The four nanopore DRS datasets for Col-0 biological replicates captured 75% (102,486) and 69%
201 104,686) of Araport11 and AtRTD2 splice site annotations, respectively. Most of the canonical
202 GU/AG splicing events (100,450; 81%) detected in the error-corrected nanopore data were found in
203 both annotations and were supported by Illumina RNAseq (Figure 4B, Supplementary table 3). A
204 total of 3,234 unique canonical splicing events in the error-corrected nanopore DRS data were
205 supported by Illumina RNAseq but absent from both Araport11 and AtRTD2 annotations,
206 highlighting potential gaps in our understanding of the complexity of Arabidopsis splicing annotation
207 (Figure 4B, Supplementary table 3). Consistent with this, we validated three of these splicing events
208 using RT-PCR (Polymerase Chain Reaction) followed by cloning and sequencing (Supplementary
209 figure 4A). In order to examine the features of these unannotated splices, we applied previously
210 determined splice site position weight matrices of the flanking sequences to categorize U2 or U12
211 class splice sites[28]. Of the 3,234 novel GU/AG events found in error-corrected data and supported by
212 Illumina alignments, 74% were classified as canonical U2 or U12 splice sites, suggesting that they are
213 authentic (Supplementary figure 4B).
214 In addition to previously unannotated splicing events, we identified unannotated
215 combinations of previously established splice sites. For example, we identified 19 *FLM* splicing
216 patterns that adhered to known splice junction sites (Figure 4A). However, 11 of these transcript
217 isoforms were not previously annotated. In order to investigate this phenomenon transcriptome-
218 wide, we analysed the 5′ cap-dependent nanopore DRS datasets of full-length mRNAs
219 (Supplementary table 1). Unique sets of co-splicing events were extracted from error-corrected
220 reads (so as to focus on splicing, we did not consider single exon reads or 5′ and 3′ positions). In

total, 13,064 unique splicing patterns were detected that matched annotations in Araport11, AtRTD2 or both (Figure 4C). Another 8,659 unique splicing patterns were identified that were not present in either annotation (Figure 4C, Supplementary table 3). Of these, 50% (4,293) used only splice donor and acceptor pairs that were already annotated in either Araport11 or AtRTD2. Hence, this approach defines splicing patterns (including retained introns) produced from alternative combinations of known splice sites.

Overall, we conclude that nanopore DRS can reveal a greater complexity of splicing in the context of full-length mRNAs compared with short-read data. However, accurate splice pattern detection benefits from error correction with, for example, high-accuracy orthogonal short-read sequencing data. However, even with error-free sequences, accurate splice detection can be confounded by the existence of equivalent alternative junctions[29]. Therefore, improved computational tools are required, not only for error correction but also for splicing-aware long-read alignment.

Differential error site analysis reveals the m^{6}A epitranscriptome

The epitranscriptome has emerged recently as a crucial, but relatively neglected, layer of gene regulation[1,2]. m^{6}A has been mapped transcriptome-wide using approaches based on antibodies that recognize this mark[6,30]. However, in principle, m^{6}A can be detected by nanopore DRS[8]. Since m^{6}A is not included in the training data for nanopore base-calling software, we asked whether its incorrect interpretation could be used to identify Arabidopsis m^{6}A transcriptome-wide. For this, we applied nanopore DRS to four biological replicates of an Arabidopsis mutant defective in the function of Virilizer (*vir-1*), a conserved m^{6}A writer complex component, and four biological replicates of a line expressing VIR fused to Green Fluorescent Protein (GFP) that restores VIR activity in the *vir-1* mutant background[9] (Supplementary figure 5A). In parallel, we sequenced a set of six biological replicates with Illumina RNAseq. We then used a G-test statistical analysis to determine whether there was a

differential error profile in alignments at each reference base between the mutant (defective m^{6}A) and VIR-complemented lines. We identified 17,491 sites with a more than two-fold higher error rate (compared with the TAIR10 reference base) in the VIR-complemented line with restored m^{6}A (Figure 5A). No VIR-dependent error sites mapped to either chloroplast or mitochondrial-encoded RNAs. In all, 99.8% of the differential error sites mapped within Araport11 annotated protein-coding genes. Motif analysis of these error sites revealed the DRAYH sequence (D=G or U or A, R=G or A, Y=C or U, H=A or C or U; Figure 5B, E value=3.3×10^{-191}), which closely resembles the established m^{6}A target consensus[1,2]. In addition, like the established location of m^{6}A sites in mRNAs[1,2], the error sites were preferentially found in 3′UTRs (Figure 5C). Since approximately 5 nt contribute to the observed current at a given time point in nanopore sequencing[8], the presence of a methylated adenosine could affect the accuracy of base-calling for the surrounding nucleotides. Consistent with this, we identified 4,749 sequences matching the motif discovered at error sites (False Discovery Rate [FDR] < 0.1; Supplementary figure 5B), with a median of two error sites per motif (95% CIs [1, 7]). Overall, these results agree with the established and conserved properties of authentic m^{6}A sites[1,2], suggesting that differential error sites can be used to identify thousands of m^{6}A modifications in nanopore DRS datasets.

In order to examine the validity of m^{6}A sites identified by the differential error site analysis, we used an orthogonal technique to map m^{6}A. Previous maps of Arabidopsis m^{6}A are based on Me-RIP[31,32] and limited by a resolution of around 200 nt[33]. Therefore, to examine Arabidopsis m^{6}A sites with a more accurate method, we used miCLIP[30] analysis of three biological replicates of Arabidopsis Col-0. We found that, like the differential error sites uncovered in the nanopore DRS analysis, the Arabidopsis miCLIP reads were enriched in 3′ UTRs but with no enrichment over stop codons (Figure 5D, Supplementary figure 5C). In all, 77% of the called nanopore DRS differential error sites fell within 5 nt of an miCLIP peak (Figure 5E, F). We therefore conclude that our analysis of nanopore data can detect authentic VIR-dependent m^{6}A sites transcriptome-wide.

Defective m^{6}A perturbs gene expression patterns and lengthens the circadian period

The combination of transcript processing and modification data obtained using nanopore DRS enabled us to investigate the impact of m^{6}A on Arabidopsis gene expression. We found a global reduction in protein-coding gene expression in *vir-1* (using either nanopore DRS or Illumina RNAseq data), corresponding to transcripts that were methylated in the VIR-complemented line (Figure 6A, Supplementary Figure 6A). These findings are consistent with the recent discovery that m^{6}A predominantly protects Arabidopsis mRNAs from endonucleolytic cleavage[32]. Therefore, although the m^{6}A writer complex comprises conserved components that target a conserved consensus sequence and distribution of m^{6}A is enriched in the last exon, it appears that this modification predominantly promotes mRNA decay in human cells[34], but mRNA stability in Arabidopsis[32].

The changes in gene expression in *vir-1* were wide ranging (Supplementary figure 6B–D). For example, we found that the abundance of mRNAs encoding components of the interlocking transcriptional feedback loops that comprise the Arabidopsis circadian oscillator[35], such as *CCA1*, were altered in *vir-1* (Supplementary figure 6B, C). This distinction was associated with a biological consequence in that the *vir-1* mutant had a lengthened clock period (Figure 6B, C). We detected m^{6}A at mRNAs encoding the clock components *CCA1*, *PRR7, GI* and *LNK1/2* in both the nanopore DRS and miCLIP data (Supplementary figure 6B). We also detected shifts in the poly(A) tail length distributions of mRNAs transcribed from genes previously shown to be under circadian control. At *CAB1* mRNAs*,* for example, we detected poly(A) tail lengths that peaked at approximately 20, 40 and 60 nt (Figure 6D). *vir-1* mutants had reduced abundance of *CAB1* mRNAs with 20 and 40 nt poly(A) tails, and an increased abundance of poly(A) tails of 60 nt in length (Figure 6D). Therefore, nanopore DRS may uncover the circadian control of poly(A) tail length, as previously reported for specific Arabidopsis genes[36]. An output of the circadian clock is the control of flowering time, and we found that not only were photoperiod pathway components differentially expressed but so too were other

296 flowering time genes (Supplementary table 4). Notably, *FLOWERING LOCUS C* (*FLC*) expression was
297 reduced by more than 40-fold compared with the wild type (Supplementary figure 6D).
298 Consequently, the proper control of circadian rhythms, flowering time and the regulatory module at
299 *FLC* ultimately requires the m^{6}A writer complex component, VIR.
300
301 *Defective m^{6}A is associated with disrupted RNA 3′ end formation*
302 In addition to measuring RNA expression, we examined the impact of m^{6}A loss on pre-mRNA
303 processing. Detectable disruptions to splicing in *vir-1* were modest. For example, using the DEX-Seq
304 software tool[37] for analysis of annotated splice sites, we found only weak effect-size changes to
305 cassette exons, retained introns or alternative donor/acceptor sites compared with the VIR-
306 complemented line in our Illumina data (Supplementary figure 6E). In contrast, a clear defect in RNA
307 3′ end formation in *vir-1* was apparent. Using a Kolmogorov–Smirnov test, we identified 3,579 genes
308 with an altered nanopore DRS 3′ position profile in the *vir-1* mutant compared with the VIR-
309 complemented line (FDR < 0.05, absolute change in position of >13 nt; Figure 6E). Of these, 3,008
310 displayed a shift to usage of more proximal poly(A) sites in *vir-1*: 60% of these genes also contain
311 m^{6}A sites detectable by nanopore DRS (compared with 32% of all expressed genes, p=1.1×10^{-266};
312 70% were detectable by miCLIP compared with 43% of all expressed genes, p=3.5×10^{-237}) and
313 correspond to locations of increased cleavage downstream of m^{6}A sites in the *vir-1* mutant
314 (Supplementary figure 6F). A total of 571 genes showed increased transcriptional readthrough
315 beyond the 3′ end in *vir-1* (Figure 6E): 73% of these loci also contained nanopore-mapped m^{6}A sites
316 (p=1.2×10^{-90}; 78% were detectable by miCLIP, p=2.1×10^{-66}). The impacts of altered 3′ processing can
317 be complex and have the potential to change the relative abundance of transcripts processed from
318 the same gene but with different coding potential. For example, we detected increased readthrough
319 of an intronic cleavage site in the Symplekin-like gene *TANG1* (*AT1G27595*; Supplementary
320 figure 6G) and increased readthrough and cryptic splicing at *ALG3* (*AT2G47760*) that also results in

chimeric RNA formation with the downstream gene *GH3.9* (*AT2G4G7750*; Figure 6F). The existence of the *ALG3-GH3.9* chimeric RNAs was supported by Illumina RNAseq (Figure 6F) and confirmed by RT-PCR, cloning and sequencing (Supplementary figure 6H). We detected 523 loci with increased levels of chimeric RNAs in *vir-1* resulting from unterminated transcription proceeding into downstream genes on the same strand. Chimeric RNAs were recently detected in mutants affecting other components of the Arabidopsis m^{6}A writer complex, MTA and FIP37[38]. However, only 33% of upstream genes forming the chimeric RNAs had detectable m^{6}A sites in the VIR-complemented line with restored VIR activity. Consequently, these findings might be explained either by an m^{6}A-independent role for VIR (or the writer complex) in 3′ end formation or an indirect effect on factors required for 3′ processing. m^{6}A independent roles for the human m^{6}A methyltransferases METTL3[39] and METTL16[40] have been found previously, and a role for the writer complex in controlling Arabidopsis RNA processing independent of m^{6}A cannot be overlooked[40]. In mammals, recognition of the canonical poly(A) signal AAUAAA involves direct binding by CPSF30[41,42]. Notably, alternative polyadenylation controls the expression of an Arabidopsis CPSF30 isoform that encodes a YT521-B homology (YTH) domain with the potential to bind and read m^{6}A[43]. A recent study indicated that this YTH domain-containing isoform is required to supress chimera formation[38]. Consequently, in plants, m^{6}A may also contribute to the recognition of specific RNA 3′ ends.

Concluding remarks

We have shown that nanopore DRS has the potential to refine multiple features of Arabidopsis genome annotation and to generate the clearest map to date of m^{6}A locations, despite the genome sequence being available since 2000[44]. Modern agriculture is dominated by a handful of intensely researched crops[45], but to diversify global food supply, enhance agricultural productivity and tackle malnutrition there is a need to focus on crops utilized in rural societies that have received little attention for crop improvement[46]. Based on our experience with Arabidopsis, we anticipate that the

346 combination of nanopore DRS and other sequencing approaches will improve genome annotation.
347 Consistent with this, we recently applied nanopore DRS to refine the annotation of water yam
348 (*Dioscorea alata*), an African orphan crop. Indeed, we are moving into an era where thousands of
349 genome sequences are available and programmes such as the Earth BioGenome Project aim to
350 sequence all eukaryotic life on Earth[47]. However, genome sequences provide only part of the puzzle:
351 annotating what they encode will be essential for us to fully utilize this information.
352
353 **Materials and methods**
354 **Plants**
355 *Plant material and growth conditions*
356 Wild-type *A. thaliana* accession Col-0 was obtained from Nottingham Arabidopsis Stock Centre. The
357 *vir-1* and VIR-complemented (*VIR::GFP-VIR*) lines were provided by K. Růžička, Brno[48]. The *hen2–2*
358 (Gabi_774HO7) mutant was provided by D. Gagliardi, Strasbourg. Seeds were sown on MS10
359 medium plates, stratified at 4°C for 2 days, germinated in a controlled environment at 22°C under
360 16-h light/8-h dark conditions and harvested 14 days after transfer to 22°C.
361
362 *Clock phenotype analysis*
363 Clock phenotype experiments were performed as previously described by measuring delayed
364 fluorescence as a circadian output[49]. Briefly, plants were grown in 12-h light/12-h dark cycles at 22°C
365 and 80 µmol m^{-2} sec^{-1} light for 9 days. Next, delayed fluorescence measurements were recorded
366 every hour for 6 days at constant temperature (22°C) and constant light (20 µmol m^{-2} sec^{-1} red light
367 and 20 µmol m^{-2} sec^{-1} blue light mix). Fast Fourier Transform (FFT) non-linear least-squares fitting to
368 estimate period length was conducted using Biodare[50].
369
370 **RNA**

RNA isolation

Total RNA was isolated using RNeasy Plant Mini kit (Qiagen) and treated with TURBO DNase (Thermo Fisher Scientific). The total RNA concentration was measured using a Qubit 1.0 Fluorometer and Qubit RNA BR Assay Kit (Thermo Fisher Scientific), and RNA quality and integrity were assessed using a NanoDrop 2000 spectrophotometer (Thermo Fisher Scientific) and Agilent 2200 TapeStation System (Agilent).

mGFP in vitro transcription

The mGFP coding sequence was amplified using CloneAmp HiFi PCR Premix (Clontech) and a forward primer containing the T7 promoter sequence (Merck; Supplementary table 5). The PCR product was purified using GeneJET Gel Extraction (Thermo Fisher Scientific) and DNA Cleanup Micro (Thermo Fisher Scientific) kits, according to the manufacturer's instructions. mGFP was *in vitro* transcribed using a mMESSAGE mMACHINE T7 ULTRA Transcription Kit (Thermo Fisher Scientific) with and without the anti-reverse cap analogue, according to the manufacturer's instructions. mGFP transcripts were treated with TURBO DNase, polyA-tailed using *Escherichia coli* poly(A) Polymerase (E-PAP) and ATP (Thermo Fisher Scientific), and recovered using a MEGAclear kit (Thermo Fisher Scientific) according to the manufacturer's instructions. The quantity of mGFP mRNAs was measured using a Qubit 1.0 Fluorometer (as described above), and the quality and integrity was checked using the NanoDrop 2000 spectrophotometer and agarose-gel electrophoresis. *In vitro* capped and non-capped mGFP mRNAs were used to prepare the library for DRS using nanopores.

RT-PCR and RT-qPCR

Total RNA was reverse transcribed using SuperScript III polymerase or SuperScript IV VILO Master Mix (Thermo Fisher Scientific) according to the manufacturer's protocol. For RT-PCR, reactions were performed using the Advantage 2 Polymerase Mix (Clontech) using the primers (Merck) listed in

Supplementary table 5. PCR products were gel purified using GeneJET Gel Extraction and DNA Cleanup Micro kits (Thermo Fisher Scientific), cloned into the pGEM T-Easy vector (Promega; according to the manufacturer's instruction) and sequenced. For RT-qPCR, reactions were carried out using the SYBR Green I (Qiagen) mix with the primers (Merck) listed in Supplementary table 5, following manufacturer's instructions.

Illumina RNA sequencing

Preparation of libraries for Illumina RNA sequencing

Illumina RNA sequencing libraries from purified mRNA were prepared and sequenced by the Centre for Genomic Research at University of Liverpool using the NEBNext Ultra Directional RNA Library Prep Kit for Illumina (New England Biolabs). Paired-end sequencing with a read length of 150 bp was carried out on an Illumina HiSeq 4000. Illumina RNA libraries from ribosome-depleted RNA were prepared using the TruSeq Stranded Total RNA with Ribo-Zero Plant kit (Illumina). Paired-end sequencing with a read length of 100 bp was carried out on an Illumina HiSeq 2000 at the Genomic Sequencing Unit of the University of Dundee. ERCC RNA Spike-In mixes (Thermo Fisher Scientific)[11,51] were included in each of the libraries using concentrations advised by the manufacturer.

Mapping of Illumina RNA sequencing data

Reads were mapped to the TAIR10 reference genome with Araport11 reference annotation using STAR version 2.6.1[52], a maximum multimapping rate of 5, a minimum splice junction overhang of 8 nt (3 nt for junctions in the Araport11 reference), a maximum of five mismatches per read and intron length boundaries of 60–10,000 nt.

Differential gene expression analysis using Illumina RNA sequencing data

Transcript-level counts for Illumina RNA sequencing reads were estimated by pseudoalignment with Salmon version 0.11.2[53]. Counts were aggregated to gene level using tximport[54] and differential gene expression analyses for *vir-1* mutant vs wild type and *vir-1* mutant vs the VIR-complemented line were conducted in R version 3.5 using edgeR version 3.24.3[55].

Differentially expressed region analysis using Illumina RNA sequencing data

Mapped read pairs originating from the forward and reverse strands were separated and coverage tracks were generated using samtools version 1.9[56]. Coverage tracks were then used as input for DERfinder version 1.16.1[57]. Expressed regions were identified using a minimum coverage of 10 reads, and differential expression between the *vir-1* and VIR-complemented lines was assessed using the analyseChr method with 50 permutations.

Differential exon usage analysis using Illumina RNA sequencing data

Annotated gene models from Araport11 were divided into transcript chunks (i.e. contiguous regions within which each base is present in the same set of transcript models). Read counts for each chunk were generated using bedtools version 2.27.1[58] intersect in count mode. Chunk counts were then processed using DEXseq version 1.28.3[37] to identify differentially expressed chunks between *vir-1* and VIR-complemented lines, using an absolute log-fold-change threshold of 1 and an FDR threshold of 0.05. Chunks were annotated as 5′ variation if they included a start site of any transcript and as 3′ variation if they contained a termination site. Chunks representing overhangs from alternative donor or acceptor sites were also classified separately. Internal exons were subclassified as a cassette exon if they could be wholly contained within any intron.

Nanopore DRS

444 *Preparation of libraries for direct RNA sequencing using nanopores*

445 mRNA was isolated from approximately 75 µg of total RNA using the Dynabeads mRNA purification
446 kit (Thermo Fisher Scientific) following the manufacturer's instructions. The quality and quantity of
447 mRNA was assessed using the NanoDrop 2000 spectrophotometer (Thermo Fisher Scientific).
448 Nanopore libraries were prepared from 1 µg poly(A)+ RNA combined with 1 µl undiluted ERCC RNA
449 Spike-In mix (Thermo Fisher Scientific) using the nanopore DRS Kit (SQK-RNA001, Oxford Nanopore
450 Technologies) according to manufacturer's instructions. The poly(T) adapter was ligated to the
451 mRNA using T4 DNA ligase (New England Biolabs) in the Quick Ligase reaction buffer (New England
452 Biolabs) for 15 min at room temperature. First-strand cDNA was synthesized by SuperScript III
453 Reverse Transcriptase (Thermo Fisher Scientific) using the oligo(dT) adapter. The RNA–cDNA hybrid
454 was then purified using Agencourt RNAClean XP magnetic beads (Beckman Coulter). The sequencing
455 adapter was ligated to the mRNA using T4 DNA ligase (New England Biolabs) in the Quick Ligase
456 reaction buffer (New England Biolabs) for 15 min at room temperature followed by a second
457 purification step using Agencourt beads (as described above). Libraries were loaded onto R9.4
458 SpotON Flow Cells (Oxford Nanopore Technologies) and sequenced using a 48-h run time.

459 To incorporate cap-dependent ligation of a biotinylated 5′ adapter RNA, the following
460 modifications were introduced into the library preparation protocol. First, 4 µg mRNA was de-
461 phosphorylated by calf intestinal alkaline phosphatase (Thermo Fisher Scientific) and the 5′ cap was
462 removed by Cap-Clip Acid Pyrophosphatase (Cambio) according to the manufacturer's instructions.
463 Next, the 5′ RNA oligo biotinylated at the 5′ end (Integrated DNA Technologies) was ligated to
464 dephosphorylated, de-capped mRNA using T4 RNA ligase I (New England Biolabs) and mRNA was
465 purified using Dynabeads MyOne Streptavidin C1 beads (Thermo Fisher Scientific) according to the
466 manufacturer's instructions. mRNA was assessed for quality and quantity using the NanoDrop 2000
467 spectrophotometer and used for nanopore DRS library preparation (as described above).

468

469 *Processing of nanopore DRS data*

470 Reads were basecalled with Guppy version 2.3.1 (Oxford Nanopore Technologies) using default RNA
471 parameters and converted from RNA to DNA fastq using seqkit version 0.10.0[59]. Reads were aligned
472 to the TAIR10 *A. thaliana* genome[60] and ERCC RNA Spike-In sequences[11,51] using minimap2 version
473 2.8[13] in spliced mapping mode using a kmer size of 14 and a maximum intron size of 10,000 nt.
474 Sequence Alignment/Map (SAM) and BAM file manipulations were performed using samtools
475 version 1.9[56].

476 Proovread version 2.14.1[14] was used to correct errors in the nanopore DRS reads[15]. Each
477 nanopore DRS replicate was split into 200 chunks for parallel processing. Each chunk was corrected
478 using four samples of Illumina poly(A) RNAseq data selected randomly from the 36 Illumina files (six
479 biological replicates sequenced across six lanes). Illumina reads 1 and 2 were merged into fragments
480 using FLASH version 1.2.11[61]. Unjoined pairs were discarded. Error correction with proovread was
481 conducted in sampling-free mode using a minimum nanopore read length of 50 nt. Since both the
482 Illumina RNAseq and nanopore DRS datasets were strand specific, proovread was modified to
483 prevent opposite strand mapping between the datasets. Corrected reads were then mapped to the
484 Araport11 reference genome using minimap2 (as described above). All figures showing gene tracks
485 with nanopore DRS reads use error-corrected reads.

486

487 *Error profile analysis using nanopore DRS data*

488 Error rate analysis of aligned reads was conducted on ERCC RNA Spike-In mix controls using pysam
489 version 0.15.2[62] for BAM file parsing. Matches, mismatches, insertions and deletions relative to the
490 reference were extracted from the cs tag (a more informative version of CIGAR string, output by
491 minimap2) and normalised by the aligned length of the read. Reference bases and mismatch bases
492 per position were also recorded and used to assess the frequency of each substitution and indel type
493 by reference base.

494

495 *Over-splitting analysis of nanopore DRS data*

496 To identify read pairs resulting from over-splitting of the signal originating from a single RNA
497 molecule, the sequencing summary files produced by Guppy were parsed for sequencing time and
498 channel identifier and then used to identify pairs of consecutively sequenced reads. Genomic
499 locations of reads were parsed from minimap2 mappings, and consecutively sequenced reads with
500 adjacent alignment within a genomic distance of –10 nt to 1,000 nt were identified. Samples
501 sequenced before or during May 2018 had very low levels of over-splitting (between 0.01% and
502 0.05% of reads) compared with those sequenced in September 2018 onwards (between 0.8% and
503 1.5% of reads).

504

505 *Analysis of the potential for internal priming in nanopore DRS data*

506 To determine whether internal priming caused by the RT step can occur in nanopore data, the
507 location of oligo(A) hexamers within Arabidopsis coding sequence (CDS) regions (Araport11) was
508 determined and reads that terminated within a 20 nt window of each hexamer were counted. Of the
509 10,116 CDS oligo(A) runs, 160 (1.58%) had at least one supporting read in one Col-0 nanopore
510 dataset. Of these, 137 were supported by only one replicate, and only four were supported by all
511 four biological replicates. In total, 66 (41%) occurred in Araport11-annotated terminal exons,
512 suggesting that they may be genuine sites of 3' end formation.

513

514 *Poly (A) length estimation using nanopore DRS data*

515 Poly (A) tail length estimations were produced using nanopolish version 0.11.0[18] and added as tags
516 to BAM files using pysam version 0.15.2[62]. Per gene length distributions were then produced using
517 Araport11 annotation, and genes with significant changes in length distribution in the *vir-1* mutant

compared with the VIR-complemented line were identified using a Kolmogorov–Smirnov test. *p*-values were adjusted for multiple testing using Benjamini-Hochberg correction.

3′ end analyses of nanopore and Helicos reads

Helicos data were prepared as previously described[20,63]. Positions with three or more supporting reads were considered to be peaks of nanopore or Helicos 3′ ends. The distance between each nanopore peak and the nearest Helicos peak was then determined. In all, 37% of nanopore peaks occurred at the same position as a Helicos peak, and the standard deviation in distance was 12.5 nt. To determine the percentage of nanopore DRS 3′ ends mapping within annotated genic features, transcripts were first flattened into a single record per gene. Exonic annotation was given priority over intronic or intergenic annotation and CDS annotation was given priority over UTR annotation. Reads were assigned to genes if they overlapped them by >20% of their aligned length, and the annotated feature type of the 3′ end position was determined. Counts were generated both for all reads and for unique positions per gene.

Isoform collapsing of nanopore DRS data

Error-corrected full-length alignments were collapsed into clusters of reads with identical sets of introns. These clusters were then subdivided by 3′ end location by using a Gaussian kernel with sigma of 100 to find local minima between read ends, which were used as cut points to separate clusters. The read with the longest aligned length in each cluster was used as the representative in the figure.

Splicing analysis of nanopore DRS and Illumina RNAseq data

Splice junction locations, their flanking sequences and the read counts supporting them were extracted from Illumina RNA sequencing, nanopore DRS and nanopore error-corrected DRS reads

using pysam version 0.14[62], as well as from Araport11[64] and AtRTD2[25] reference annotations. Splice junctions at the same position but on the opposite strand were counted independently. Junctions were classified by their most likely snRNP machinery using Biopython version 1.71[65], with position weight matrices as previously calculated[28]. Position weight matrices were scored against the sequence –3 nt to +10 nt of the donor site and –14 nt to +3 nt of the acceptor site. Position weight matrix scores greater than zero indicate a match to the motif, while scores of around zero, or negative scores, indicate background frequencies or deviation from the motif. Positive scores were normalized into the range 50–100 as done previously[28]. Junctions with U12 donor scores of >75 and U12 acceptor scores of >65 were classified as U12 junctions, while junctions with U2 donor and acceptor scores of >60 were classified as U2, as done previously[25]. Junctions were further categorized as canonical or non-canonical based on the presence or absence, respectively, of GT/AG intron border sequences. For isoform analysis, linked splices from the same read were extracted from full-length nanopore error-corrected reads and counted to create unique sets of splice junctions. Intronless reads were not counted. UpSet plots were generated in Python 3.6 using the package upsetplot[66].

Validation of novel splice sites

To validate novel splice junctions detected in nanopore DRS, five splice sites out of the 20 most highly expressed splice sites were selected for further validation; three of the five selected splice sites were successfully amplified in RT-PCR followed by Sanger sequencing (described above).

5′ adapter detection analyses using nanopore DRS data

To produce positive and negative examples of 5′ adapter-containing sequences, 5′ soft-clipped regions were extracted from aligned reads for the Col-0 replicate 1 datasets (with and without adapter ligation) using pysam[62]. These soft-clipped sequences were then searched for the presence

of the GeneRacer adapter sequence using BLASTN version 2.7.1[67]. Two rules were initially applied to filter BLASTN results: a match of 10 nt or more to the 44 nt adapter, and an E value of <100. Reads from the adapter-containing dataset that failed one or both criteria were used as negative training examples. A final rule requiring the match to the adapter sequence to occur directly adjacent to the aligned read was also applied. Reads from the adapter-containing dataset that passed all three rules were used as the positive training set. When comparing the ratio of positive to negative examples between datasets containing the adapter and those generated from the same tissue but without the adapter, we found that these three rules gave a signal-to-noise ratio of >5,000 (Supplementary table 2).

In all, 72,083 positive and 123,739 negative training examples from Col-0 tissue replicate 1 were collected to train the neural network. We then estimated the amount of raw signal from the 5′ end of the squiggle that was required on average to capture the 5′ adapter. To do this, we used nanopolish eventalign version 0.11.0[68] to identify the interval in the raw read corresponding to the mRNA alignment to the reference in the positive examples of 5′ adapter-containing sequences. Since the adapter can be identified immediately adjacent to the alignment in sequence space for these reads, the signal after the event alignment should correspond to the signal originating from the adapter. The median length of these signals was 1,441 points, and 96% of the signals were <3,000 points. Therefore, we used a window size of 3,000 to make predictions.

The model was trained in Python 3.6 using Keras version 2.2.4 with the Tensorflow version 1.10.0 backend[69,70]. A ResNet-style architecture was used[71], composed of eight residual blocks containing two convolutional layers of kernel size 5 and a shortcut convolution with kernel size 1. Down-sampling using maximum pooling layers with a stride of 2 was used between each residual block. A penultimate densely connected layer of size 16 was used, with training dropout of 0.5. Input signals were standardized by median absolute deviation scaling across the whole read before the final 3,000 points were taken, and the negative samples were augmented by addition of random

internal signals from reads and pure Gaussian, multi-Gaussian and perlin noise signals[72]. The whole dataset was also augmented on the fly during training by the addition of Gaussian noise with a standard deviation of 0.1. Models were trained for a maximum of 100 epochs (batch size of 128, 100 batches per epoch, positive and negative examples sampled in a 1:1 ratio) using the RMSprop optimizer with an initial learning rate of 0.001, which was reduced by a factor of 10 after three epochs with no reduction in validation loss. Early stopping was used after five epochs with no reduction in validation loss. We found that a number of negative training examples from the ends of reads, but not from internal positions, were likely to be incorrectly labelled by the BLASTN method, because the model predicted them to contain adapters. We therefore filtered these to clean the training data, before repeating the training process. Model performance was evaluated using five-fold cross validation and by testing on independently generated datasets from Col-0 replicate 2, produced with and without the adapter ligation protocol (Supplementary figure 3B, C)[69,70].

To evaluate the reduction in 3′ bias of adapter-ligated datasets, we used Araport11 exon annotations to produce per base coverage for each gene in the Col-0 replicate 2 dataset. Coverage was generated separately for reads predicted to contain adapters and for those predicted not to contain adapters. Leading zeros at the extreme 5′ and 3′ ends of genes were assumed to be caused by mis-annotation of UTRs and so were trimmed. The quartile coefficient of variation (interquartile range / median) was then used as a robust measure of variation in coverage across each gene. To validate the 5′ ends of adapter-ligated reads with orthogonal data, full-length cDNA clone sequences were downloaded from RIKEN RAFL (Arabidopsis full-length cDNA clones)[23]. These were mapped with minimap2[13] in spliced mode. The distance from each nanopore alignment 5′ end to the nearest RIKEN RAFL alignment[23]. 5′ end was calculated using bedtools[58]. The amount of 5′ end sequence that is rescued when 5′ adapters are used was estimated by identifying the largest peak in 5′ end locations per gene in the absence of adapter, and then measuring how this peak shifted using reads predicted to contain adapters.

618

619 *Differential error site analysis using nanopore DRS data*

620 To detect sites of Virilizer-dependent m^{6}A RNA modifications, we developed scripts to test changes
621 in per base error profiles of aligned reads. Pileup columns for each position with coverage of >10
622 reads were generated using pysam[62] and reads in each column were categorized as either A, C, G, T
623 or indel. The relative proportions of each category were counted. Counts from replicates of the
624 same experimental condition were aggregated and a 2×5 contingency table was produced for each
625 base comparing *vir-1* and VIR-complemented lines. A G-test was performed to identify bases with
626 significantly altered error profiles. For bases with a *p*-value of <0.05, G-tests for homogeneity
627 between replicates of the same condition were then performed. Bases where the sum of the G
628 statistic for homogeneity tests was greater than the G statistic for the *vir-1* and VIR-complemented
629 line comparison were filtered. Multiple testing correction was carried out using the Benjamini-
630 Hochberg method, and an FDR threshold of 0.05 was used. The $\log_2$ fold change in mismatch to
631 match ratio (compared with the reference base) between the *vir-1* and VIR-complemented lines was
632 calculated using Haldane correction for zero counts. Bases that had a log fold change of >1 were
633 considered to have a reduced error rate in the *vir-1* mutant.

634 To identify motifs enriched at sites with a reduced error rate, reduced error rate sites were
635 increased in size by 5 nt in each direction and overlapping sites were merged using bedtools version
636 2.27.1[58]. Sequences corresponding to these sites were extracted from the TAIR10 reference and
637 over-represented motifs were detected in the sequences using MEME version 5.0.2[73], run in zero or
638 one occurrence mode with a motif size range of 5–7 and a minimum requirement of 100 sequence
639 matches. The presence of these motifs at error sites was then detected using FIMO version 5.0.2[74]. A
640 relaxed FDR threshold of 0.1 was used with FIMO to capture more degenerate motifs matching the
641 m^{6}A consensus.

642

643 *Differential gene expression analysis using nanopore DRS data*

644 Gene level counts were produced for each nanopore DRS replicate using featureCounts version
645 1.6.3[75] in long-read mode with strand-specific counting. Differential expression analysis between the
646 *vir-1* and VIR-complemented lines was then performed in R version 3.5 using edgeR version 3.24.3[55].
647

648 *Identification of alternative 3′ end positions and chimeric RNA using nanopore DRS data*
649 Genes with differential 3′ end usage were identified by producing 3′ profiles of reads which
650 overlapped with each annotated gene locus by >20%. These profiles were then compared between
651 the *vir-1* and VIR-complemented lines using a Kolmogorov–Smirnov test to identify changes.
652 Multiple testing correction was performed using the Benjamini-Hochberg method. To approximately
653 identify the direction and distance of the change, the normalized single base level histograms of the
654 VIR-complemented line profile was subtracted from that of the mutant profile, and the minimum
655 and maximum points in the difference profile were identified. These represent the sites of most
656 reduced and increased relative usage, respectively. Results were filtered for an FDR of <0.05 and
657 absolute change of site >13 nt (the measured error range of nanopore DRS 3′ end alignment). The
658 presence of m^{6}A modifications at genes with differential 3′ end usage was assessed using bedtools
659 intersect[58], and significant enrichment of m^{6}A at these genes was tested using a hypergeometric test
660 (using all expressed genes as the background population).
661 To identify genes with a significant increase in chimeras in the *vir-1* mutant, we used
662 Araport11 annotation[64] to identify reads that overlapped with multiple adjacent gene loci (i.e.
663 chimeric reads) and those originating from a single locus (i.e. non-chimeric reads). To reduce false
664 positives caused by reads mapping across tandem duplicated loci, reads mapping to genes
665 annotated in PTGBase[76] were filtered out. Chimeric reads were considered to originate from the
666 most upstream gene with which they overlapped. We pooled reads from replicates for each
667 experimental condition and used 50 bootstrapped samples (75% of the total data without

replacement) to estimate the ratio of chimeric to non-chimeric reads at each gene in each condition. Haldane correction for zero counts was applied. The distributions of chimeric to non-chimeric ratios in the *vir-1* and VIR-complemented lines were tested using a Kolmogorov–Smirnov test to detect loci with altered chimera production. All possible pairwise combinations of VIR-complemented and *vir-1* bootstraps were then compared to produce a distribution of estimates of change in the chimeric to non-chimeric ratio in the *vir-1* mutant. Loci that had more than one chimeric read in *vir-1*, demonstrated at least a two-fold increase in the chimeric read ratio in >50% of bootstrap comparisons and were significantly changed at a FDR of <0.05 were considered to be sites of increased chimeric RNA formation in the *vir-1* mutant.

miCLIP

Preparation of miCLIP libraries

Total RNA for miCLIP was isolated from 7.5 mg of 14-day old Arabidopsis Col-0 seedlings as previously described[77]. mRNA was isolated from ~1 mg total RNA using oligo(dT) and streptavidin paramagnetic beads (PolyATtract mRNA Isolation Systems, Promega) according to the manufacturer's instructions. miCLIP was carried out using 15 µg mRNA as previously described[78] using an antibody against N6-methyladenosine (#202 003 Synaptic Systems), with minor modifications. No-antibody controls were processed throughout the experiment. RNA-antibody complexes were separated by 4–12% Bis-Tris gel electrophoresis at 180 V for 50 min and transferred to nitrocellulose membranes (Protran BA85 0.45µm, GE Healthcare) at 30 V for 60 min. Membranes were then exposed to Medical X-Ray Film Blue (Agfa) at −80°C overnight. Reverse transcription was carried out using barcoded RT primers: RT41, RT48, RT49 and RT50 (Integrated DNA Technologies; Supplementary table 5). After reverse transcription, one cDNA fraction corresponding to 70–200 nt was gel purified after 6% TBE-urea gel electrophoresis (Thermo Fisher Scientific). After the final PCR step, all libraries were pooled together, purified using Agencourt Ampure XP magnetic beads

693 (Beckman Coulter) and eluted in nuclease-free water. Paired-end sequencing with a read length of
694 100 bp was carried out on an Illumina MiSeq v2 at Edinburgh Genomics, University of Edinburgh.
695 Input sample libraries were prepared using NEBNext Ultra Directional RNA Library Prep Kit for
696 Illumina (New England Biolabs) and sequenced on an Illumina HiSeq2000 at the Tayside Centre for
697 Genomics Analysis, University of Dundee, with a pair-end read length of 75 bp.
698
699 *Processing of miCLIP sequencing data*
700 miCLIP data were assessed for quality using FastQC version 0.11.8[79] and MultiQC version 1.7[80]. Only
701 the forward read was used for analysis because the miCLIP site is located at the 5′ position of the
702 forward read. 3′ adapter and poly(A) sequences were trimmed using cutadapt version 1.18[81] and
703 unique molecular identifiers were extracted from the 5′ end of the reads using UMI-tools version
704 0.5.5[82]. Immunoprecipitation and no-antibody controls were demultiplexed and multiplexing
705 barcodes were trimmed using seqkit version 0.10.0[59]. Reads were mapped to the TAIR10 reference
706 genome with Araport11 reference annotation[64] using STAR version 2.6.1[52], a maximum
707 multimapping rate of 5, a minimum splice junction overhang of 8 nt (3 nt for junctions in the
708 Araport11 reference), a maximum of five mismatches per read, and intron length boundaries of 60–
709 10,000 nt. SAM and BAM file manipulations were performed using samtools version 1.9[56]. Removal
710 of PCR duplicates was then performed using UMI-tools in a directional model[82]. miCLIP 5′ coverage
711 and matched input 5′ coverage tracks were generated using bedtools version 2.27.1[58] and these
712 were used to call miCLIP peaks at single nucleotide resolution with Piranha version 1.2.1[83] and
713 relaxed *p*-value thresholds of 0.5. Reproducible peaks across pairwise combinations of the three
714 replicates were identified by irreproducible discovery rate (IDR) analysis using Python package idr
715 version 2.0.3 with an IDR threshold of 0.05[84]. The final set of peaks was identified by pooling the
716 three replicates, re-analysing using Piranha, ranking the peaks by FDR and selecting the top N peaks,

where N is the smallest number of reproducible peaks discovered by pairwise comparisons of the three replicates. This yielded 141,198 unique nucleotide-level miCLIP peaks.

m^{6}A liquid chromatography–mass spectroscopy analysis

m^{6}A content analysis using liquid chromatography–mass spectroscopy (LC-MS) was performed as previously described[85]. Chromatography was carried out by the FingerPrints Proteomics facility, University of Dundee.

Code availability

All scripts, pipelines and notebooks used for this study are available on GitHub at https://github.com/bartongroup/Simpson_Barton_Nanopore_1

Data availability

Sequencing datasets described in this study have been deposited at the European Nucleotide Archive understudy accession number PRJEB32782.

Acknowledgements

This work was funded by BBSRC grants BB/J00247X/1, BB/M004155/1, BB/M010066/1, the University of Dundee Global Challenges Research Fund and the European Union's Horizon 2020 research and innovation programme under Marie Skłodowska-Curie grant agreement No. 799300. The m^{6}A LC-MS analysis was carried out by Abdel Atrih of the FingerPrints Proteomics Facility, University of Dundee, which is supported by a Wellcome Trust Technology Platform award (097945/B/11/Z). We thank Kasper Rasmussen and Csaba Hornyik for their comments on the manuscript.

Author contributions

GGS, NJS and AVS conceived the study; KK, AVS and KM designed and performed the experiments; MTP and NJS undertook data analysis; PDG undertook the clock experiments, supervised by AH; GGS and GJB supervised the study; GGS, MTP and AVS wrote the paper. All authors read and commented on the text.

Competing interests

No competing interests declared.

References

1 Meyer, K. D. & Jaffrey, S. R. Rethinking m^{6}A readers, writers, and erasers. *Annual Review of Cell and Developmental Biology* **33**, 319-342, doi:10.1146/annurev-cellbio-100616-060758 (2017).

2 Roundtree, I. A., Evans, M. E., Pan, T. & He, C. Dynamic RNA modifications in gene expression regulation. *Cell* **169**, 1187-1200, doi:10.1016/j.cell.2017.05.045 (2017).

3 Jan, C. H., Friedman, R. C., Ruby, J. G. & Bartel, D. P. Formation, regulation and evolution of *Caenorhabditis elegans* 3 ' UTRs. *Nature* **469**, 97-101, doi:10.1038/nature09616 (2011).

4 Houseley, J. & Tollervey, D. Apparent non-canonical *trans*-splicing is generated by reverse transcriptase *in vitro*. *Plos One* **5**, doi:10.1371/journal.pone.0012271 (2010).

5 Mourão, K. *et al.* Detection and mitigation of spurious antisense expression with RoSA. *F1000Research* **8**, doi:10.12688/f1000research.18952.1 (2019).

6 Helm, M. & Motorin, Y. Detecting RNA modifications in the epitranscriptome: predict and validate. *Nat Rev Genet* **18**, 275-291, doi:10.1038/nrg.2016.169 (2017).

7 Steijger, T. *et al.* Assessment of transcript reconstruction methods for RNA-seq. *Nat Methods* **10**, 1177-1184, doi:10.1038/Nmeth.2714 (2013).

8 Garalde, D. R. *et al.* Highly parallel direct RNA sequencing on an array of nanopores. *Nature Methods* **15**, 201, doi:10.1038/nmeth.4577 (2018).

9 Ruzicka, K. *et al.* Identification of factors required for m^{6}A mRNA methylation in Arabidopsis reveals a role for the conserved E3 ubiquitin ligase HAKAI. *New Phytol* **215**, 157-172, doi:10.1111/nph.14586 (2017).

10 Lange, H. *et al.* The RNA helicases AtMTR4 and HEN2 target specific subsets of nuclear transcripts for degradation by the nuclear exosome in *Arabidopsis thaliana*. *PLoS Genet* **10**, doi:10.1371/journal.pgen.1004564 (2014).

11 Jiang, L. *et al.* Synthetic spike-in standards for RNA-seq experiments. *Genome Res* **21**, 1543-1551, doi:10.1101/gr.121095.111 (2011).

12 Reid, L. H. *et al.* Proposed methods for testing and selecting the ERCC external RNA controls. *Bmc Genomics* **6**, doi:10.1186/1471-2164-6-150 (2005).
13 Li, H. Minimap2: pairwise alignment for nucleotide sequences. *Bioinformatics* **34**, 3094-3100, doi:10.1093/bioinformatics/bty191 (2018).
14 Hackl, T., Hedrich, R., Schultz, J. & Forster, F. proovread: large-scale high-accuracy PacBio correction through iterative short read consensus. *Bioinformatics* **30**, 3004-3011, doi:10.1093/bioinformatics/btu392 (2014).
15 Depledge, D. P. *et al.* Direct RNA sequencing on nanopore arrays redefines the transcriptional complexity of a viral pathogen. *Nat Commun* **10**, 754, doi:10.1038/s41467-019-08734-9 (2019).
16 Payne, A., Holmes, N., Rakyan, V. & Loose, M. BulkVis: a graphical viewer for Oxford nanopore bulk FAST5 files. *Bioinformatics*, doi:10.1093/bioinformatics/bty841 (2018).
17 Matsui, A. *et al.* Novel stress-inducible antisense RNAs of protein-coding loci are synthesized by RNA-dependent RNA polymerase. *Plant Physiology* **175**, 457-472, doi:10.1104/pp.17.00787 (2017).
18 Workman, R. E. *et al.* Nanopore native RNA sequencing of a human poly(A) transcriptome. *bioRxiv*, 459529, doi:10.1101/459529 (2018).
19 Lima, S. A. *et al.* Short poly(A) tails are a conserved feature of highly expressed genes. *Nat Struct Mol Biol* **24**, 1057–1063, doi:10.1038/nsmb.3499 (2017).
20 Duc, C., Sherstnev, A., Cole, C., Barton, G. J. & Simpson, G. G. Transcription termination and chimeric RNA formation controlled by *Arabidopsis thaliana* FPA. *PLOS Genetics* **9**, e1003867, doi:10.1371/journal.pgen.1003867 (2013).
21 Hornyik, C., Terzi, L. C. & Simpson, G. G. The spen family protein FPA controls alternative cleavage and polyadenylation of RNA. *Developmental Cell* **18**, 203-213, doi:10.1016/j.devcel.2009.12.009.
22 Rigal, M., Kevei, Z., Pelissier, T. & Mathieu, O. DNA methylation in an intron of the *IBM1* histone demethylase gene stabilizes chromatin modification patterns. *EMBO J* **31**, 2981-2993, doi:10.1038/emboj.2012.141 (2012).
23 Seki, M. *et al.* Functional annotation of a full-length *Arabidopsis* cDNA collection. *Science* **296**, 141-145, doi:DOI 10.1126/science.1071006 (2002).
24 Ushijima, T. *et al.* Light controls protein localization through phytochrome-mediated alternative promoter selection. *Cell* **171**, 1316-1325, doi:10.1016/j.cell.2017.10.018 (2017).
25 Zhang, R. *et al.* A high quality Arabidopsis transcriptome for accurate transcript-level analysis of alternative splicing. *Nucleic Acids Res* **45**, 5061-5073, doi:10.1093/nar/gkx267 (2017).
26 Schon, M. A., Kellner, M. J., Plotnikova, A., Hofmann, F. & Nodine, M. D. NanoPARE: parallel analysis of RNA 5' ends from low-input RNA. *Genome Res* **28**, 1931-1942, doi:10.1101/gr.239202.118 (2018).
27 Pose, D. *et al.* Temperature-dependent regulation of flowering by antagonistic FLM variants. *Nature* **503**, 414-417, doi:10.1038/nature12633 (2013).
28 Sheth, N. *et al.* Comprehensive splice-site analysis using comparative genomics. *Nucleic Acids Res* **34**, 3955-3967, doi:10.1093/nar/gkl556 (2006).

29 Dehghannasiri, R., Szabo, L. & Salzman, J. Ambiguous splice sites distinguish circRNA and linear splicing in the human genome. *Bioinformatics*, doi:10.1093/bioinformatics/bty785 (2018).

30 Linder, B. *et al.* Single-nucleotide-resolution mapping of m6A and m6Am throughout the transcriptome. *Nat Methods* **12**, 767-772, doi:10.1038/nmeth.3453 (2015).

31 Shen, L. S. *et al. N*-6-methyladenosine RNA modification regulates shoot stem cell fate in Arabidopsis. *Dev Cell* **38**, 186-200, doi:10.1016/j.devcel.2016.06.008 (2016).

32 Anderson, S. J. *et al.* N^6-methyladenosine inhibits local ribonucleolytic cleavage to stabilize mRNAs in Arabidopsis. *Cell Rep* **25**, 1146-1157, doi:10.1016/j.celrep.2018.10.020 (2018).

33 Ke, S. *et al.* A majority of m6A residues are in the last exons, allowing the potential for 3' UTR regulation. *Genes Dev* **29**, 2037-2053, doi:10.1101/gad.269415.115 (2015).

34 Wang, X. *et al. N*-6-methyladenosine-dependent regulation of messenger RNA stability. *Nature* **505**, 117-120, doi:10.1038/nature12730 (2014).

35 McClung, C. R. The genetics of plant clocks. *Adv Genet* **74**, doi:10.1016/b978-0-12-387690-4.00004-0 (2011).

36 Lidder, P., Gutierrez, R. A., Salome, P. A., McClung, C. R. & Green, P. J. Circadian control of messenger RNA stability. Association with a sequence-specific messenger RNA decay pathway. *Plant Physiol* **138**, 2374-2385, doi:10.1104/pp.105.060368 (2005).

37 Anders, S., Reyes, A. & Huber, W. Detecting differential usage of exons from RNA-seq data. *Genome Research* **22**, 2008-2017, doi:10.1101/gr.133744.111 (2012).

38 Pontier, D. *et al.* The m6A pathway protects the transcriptome integrity by restricting RNA chimera formation in plants. *Life Sci Alliance* **2**, doi:10.26508/lsa.201900393 (2019).

39 Lin, S., Choe, J., Du, P., Triboulet, R. & Gregory, R. I. The m^6A methyltransferase METTL3 promotes translation in human cancer cells. *Mol Cell* **62**, 335-345, doi:10.1016/j.molcel.2016.03.021 (2016).

40 Pendleton, K. E. *et al.* The U6 snRNA m^6A methyltransferase METTL16 regulates SAM synthetase intron retention. *Cell* **169**, 824-835 e814, doi:10.1016/j.cell.2017.05.003 (2017).

41 Chan, S. L. *et al.* CPSF30 and Wdr33 directly bind to AAUAAA in mammalian mRNA 3 ' processing. *Gene Dev* **28**, 2370-2380, doi:10.1101/gad.250993.114 (2014).

42 Schonemann, L. *et al.* Reconstitution of CPSF active in polyadenylation: recognition of the polyadenylation signal by WDR33. *Gene Dev* **28**, 2381-2393, doi:10.1101/gad.250985.114 (2014).

43 Stevens, A. T., Howe, D. K. & Hunt, A. G. Characterization of mRNA polyadenylation in the apicomplexa. *Plos One* **13**, doi:10.1371/journal.pone.0203317 (2018).

44 Kaul, S. *et al.* Analysis of the genome sequence of the flowering plant *Arabidopsis thaliana*. *Nature* **408**, 796-815, doi:10.1038/35048692 (2000).

45 United Nations, D. o. E. a. S. A., Population Division. in *Working Paper No. ESA/P/WP/248* (2017).

46 Chang, Y. *et al.* The draft genomes of five agriculturally important African orphan crops. *Gigascience* **8**, doi:10.1093/gigascience/giy152 (2018).

47 Lewin, H. A. *et al.* Earth BioGenome Project: Sequencing life for the future of life. *P Natl Acad Sci USA* **115**, 4325-4333, doi:10.1073/pnas.1720115115 (2018).

48 Růžička, K. *et al.* Identification of factors required for m6A mRNA methylation in Arabidopsis reveals a role for the conserved E3 ubiquitin ligase HAKAI. *New Phytologist* **215**, 157-172, doi:10.1111/nph.14586 (2017).

49 Gould, P. D. *et al.* Delayed fluorescence as a universal tool for the measurement of circadian rhythms in higher plants. *The Plant Journal* **58**, 893-901, doi:10.1111/j.1365-313X.2009.03819.x (2009).

50 Moore, A., Zielinski, T. & Millar, A. J. in *Plant Circadian Networks: Methods and Protocols* (ed Dorothee Staiger) 13-44 (Springer New York, 2014).

51 Lee, H., Pine, P. S., McDaniel, J., Salit, M. & Oliver, B. External RNA controls consortium beta version update. *Journal of genomics* **4**, 19-22, doi:10.7150/jgen.16082 (2016).

52 Dobin, A. *et al.* STAR: ultrafast universal RNA-seq aligner. *Bioinformatics* **29**, 15-21, doi:10.1093/bioinformatics/bts635 (2013).

53 Patro, R., Duggal, G., Love, M. I., Irizarry, R. A. & Kingsford, C. Salmon provides fast and bias-aware quantification of transcript expression. *Nature Methods* **14**, 417, doi:10.1038/nmeth.4197 (2017).

54 Soneson, C., Love, M. & Robinson, M. Differential analyses for RNA-seq: transcript-level estimates improve gene-level inferences [version 2; peer review: 2 approved]. *F1000Research* **4**, doi:10.12688/f1000research.7563.2 (2016).

55 Robinson, M. D., McCarthy, D. J. & Smyth, G. K. edgeR: a Bioconductor package for differential expression analysis of digital gene expression data. *Bioinformatics* **26**, 139-140, doi:10.1093/bioinformatics/btp616 (2010).

56 Wysoker, A. *et al.* The sequence alignment/map format and SAMtools. *Bioinformatics* **25**, 2078-2079, doi:10.1093/bioinformatics/btp352 (2009).

57 Collado-Torres, L. *et al.* Flexible expressed region analysis for RNA-seq with derfinder. *Nucleic Acids Res* **45**, e9, doi:10.1093/nar/gkw852 (2017).

58 Quinlan, A. R. & Hall, I. M. BEDTools: a flexible suite of utilities for comparing genomic features. *Bioinformatics* **26**, 841-842, doi:10.1093/bioinformatics/btq033 (2010).

59 Shen, W., Le, S., Li, Y. & Hu, F. SeqKit: a cross-platform and ultrafast toolkit for FASTA/Q file manipulation. *PLOS ONE* **11**, e0163962, doi:10.1371/journal.pone.0163962 (2016).

60 The Arabidopsis Genome, I. Analysis of the genome sequence of the flowering plant *Arabidopsis thaliana*. *Nature* **408**, 796-815, doi:10.1038/35048692 (2000).

61 Magoč, T. & Salzberg, S. L. FLASH: fast length adjustment of short reads to improve genome assemblies. *Bioinformatics* **27**, 2957-2963, doi:10.1093/bioinformatics/btr507 (2011).

62 Heger, A., Belgrad, T. G., Goodson, M., & Jacobs, K. pysam: Python interface for the SAM/BAM sequence alignment and mapping format. (2014).

63 Schurch, N. J. *et al.* Improved Annotation of 3' Untranslated Regions and Complex Loci by Combination of Strand-Specific Direct RNA Sequencing, RNA-Seq and ESTs. *PLOS ONE* **9**, e94270, doi:10.1371/journal.pone.0094270 (2014).

64 Cheng, C.-Y. *et al.* Araport11: a complete reannotation of the *Arabidopsis thaliana* reference genome. *The Plant Journal* **89**, 789-804, doi:10.1111/tpj.13415 (2017).

65 Dalke, A. *et al.* Biopython: freely available Python tools for computational molecular biology and bioinformatics. *Bioinformatics* **25**, 1422-1423, doi:10.1093/bioinformatics/btp163 (2009).
66 Nothman, J. *upsetplot*, <https://github.com/jnothman/UpSetPlot> (2018).
67 Camacho, C. *et al.* BLAST+: architecture and applications. *BMC bioinformatics* **10**, 421-421, doi:10.1186/1471-2105-10-421 (2009).
68 Loman, N. J., Quick, J. & Simpson, J. T. A complete bacterial genome assembled *de novo* using only nanopore sequencing data. *Nature Methods* **12**, 733, doi:10.1038/nmeth.3444 (2015).
69 Chollet, F. *Keras*, <https://github.com/fchollet/keras> (2018).
70 Abadi, M. *et al.* TensorFlow: large-scale machine learning on heterogeneous distributed systems. (2016).
71 Kaiming He, X. Z., Shaoqing Ren, Jian Sun. Deep residual learning for image recognition. (2015).
72 Wick, R. R., Judd, L. M. & Holt, K. E. Deepbinner: Demultiplexing barcoded Oxford Nanopore reads with deep convolutional neural networks. *PLoS Comput Biol* **14**, e1006583, doi:10.1371/journal.pcbi.1006583 (2018).
73 Bailey, T. L. *et al.* MEME Suite: tools for motif discovery and searching. *Nucleic Acids Research* **37**, W202-W208, doi:10.1093/nar/gkp335 (2009).
74 Grant, C. E., Bailey, T. L. & Noble, W. S. FIMO: scanning for occurrences of a given motif. *Bioinformatics* **27**, 1017-1018, doi:10.1093/bioinformatics/btr064 (2011).
75 Liao, Y., Smyth, G. K. & Shi, W. The Subread aligner: fast, accurate and scalable read mapping by seed-and-vote. *Nucleic acids Res* **41**, e108-e108, doi:10.1093/nar/gkt214 (2013).
76 Yu, J. *et al.* PTGBase: an integrated database to study tandem duplicated genes in plants. *Database* **2015**, doi:10.1093/database/bav017 (2015).
77 Quesada, V., Macknight, R., Dean, C. & Simpson, G. G. Autoregulation of *FCA* pre-mRNA processing controls Arabidopsis flowering time. *The EMBO Journal* **22**, 3142-3152, doi:10.1093/emboj/cdg305 (2003).
78 Grozhik, A. V., Linder, B., Olarerin-George, A. O. & Jaffrey, S. R. Mapping m^6A at individual-nucleotide resolution using crosslinking and immunoprecipitation (miCLIP). *Methods in molecular biology* **1562**, 55-78, doi:10.1007/978-1-4939-6807-7_5 (2017).
79 Andrews, S. FastQC: a quality control tool for high throughput sequence data. (2010).
80 Ewels, P., Magnusson, M., Käller, M. & Lundin, S. MultiQC: summarize analysis results for multiple tools and samples in a single report. *Bioinformatics* **32**, 3047-3048, doi:10.1093/bioinformatics/btw354 (2016).
81 Martin, M. Cutadapt removes adapter sequences from high-throughput sequencing reads. **17**, 3, doi:10.14806/ej.17.1.200 (2011).
82 Smith, T., Heger, A. & Sudbery, I. UMI-tools: modeling sequencing errors in Unique Molecular Identifiers to improve quantification accuracy. *Genome research* **27**, 491-499, doi:10.1101/gr.209601.116 (2017).
83 Uren, P. J. *et al.* Site identification in high-throughput RNA-protein interaction data. *Bioinformatics* **28**, 3013-3020, doi:10.1093/bioinformatics/bts569 (2012).

84 Li, Q., Brown, J. B., Huang, H. & Bickel, P. J. Measuring reproducibility of high-throughput experiments. *Ann. Appl. Stat.* **5**, 1752-1779, doi:10.1214/11-AOAS466 (2011).

85 Huang, H. *et al.* Recognition of RNA *N*6-methyladenosine by IGF2BP proteins enhances mRNA stability and translation. *Nature Cell Biology* **20**, 285-295, doi:10.1038/s41556-018-0045-z (2018).

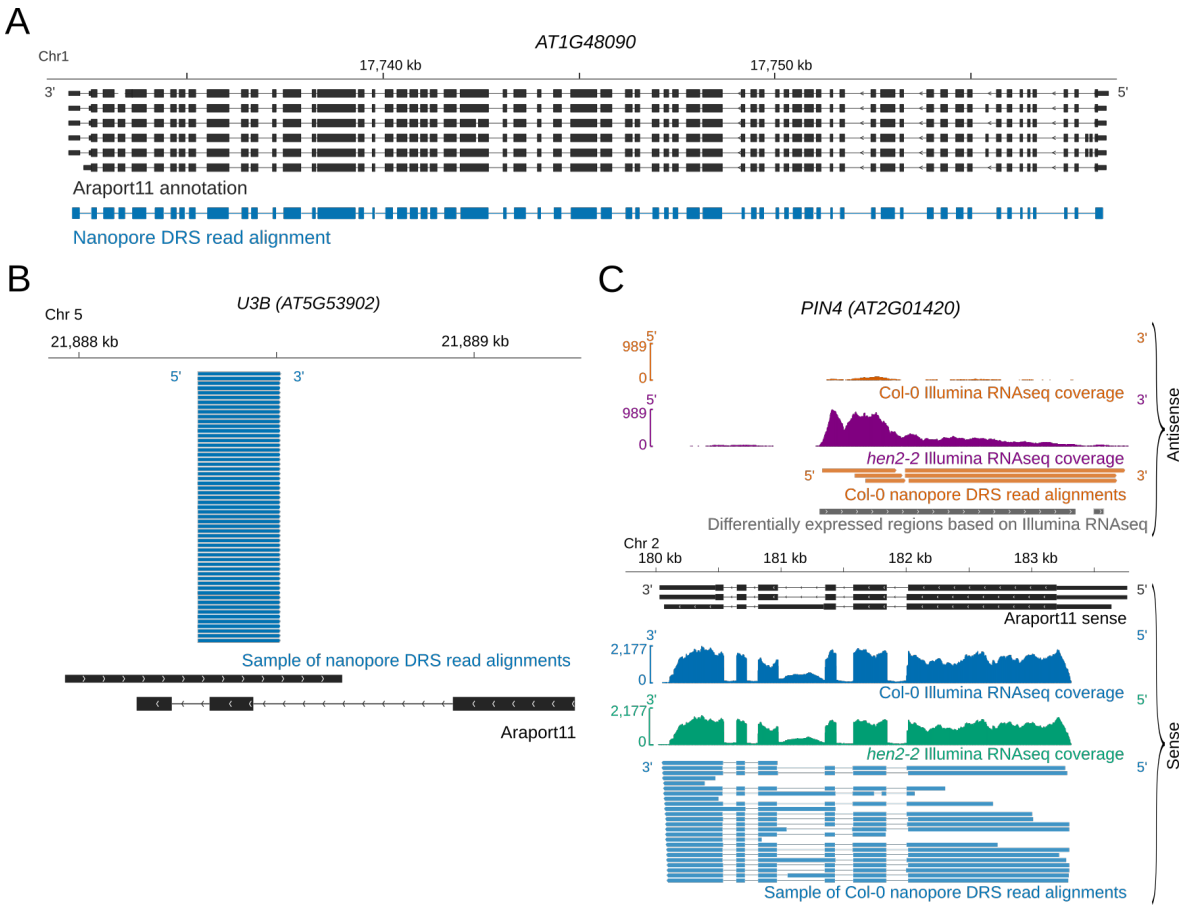

Figure 1. Diverse Arabidopsis RNAs are detected by nanopore DRS.
(**A**) Nanopore DRS 12.7-kb read alignment at *AT1G48090*, comprising 63 exons. Black, Araport11 annotation; blue, nanopore DRS read alignment.
(**B**) Nanopore DRS read alignments at the snoRNA gene *U3B*. Black, Araport11 annotation; blue, nanopore DRS read alignments.
(**C**) *PIN4* long non-coding antisense RNAs detected using nanopore DRS. Blue, Col-0 sense Illumina RNAseq coverage and nanopore sense read alignments; orange, Col-0 antisense Illumina RNAseq coverage and nanopore antisense read alignments; green, *hen2-2* mutant sense Illumina RNAseq coverage; purple, *hen2-2* mutant antisense Illumina RNAseq coverage; black, sense RNA isoforms found in Araport11; grey, antisense differentially expressed regions detected with DERfinder.
[Linked to Supplementary figure 1].

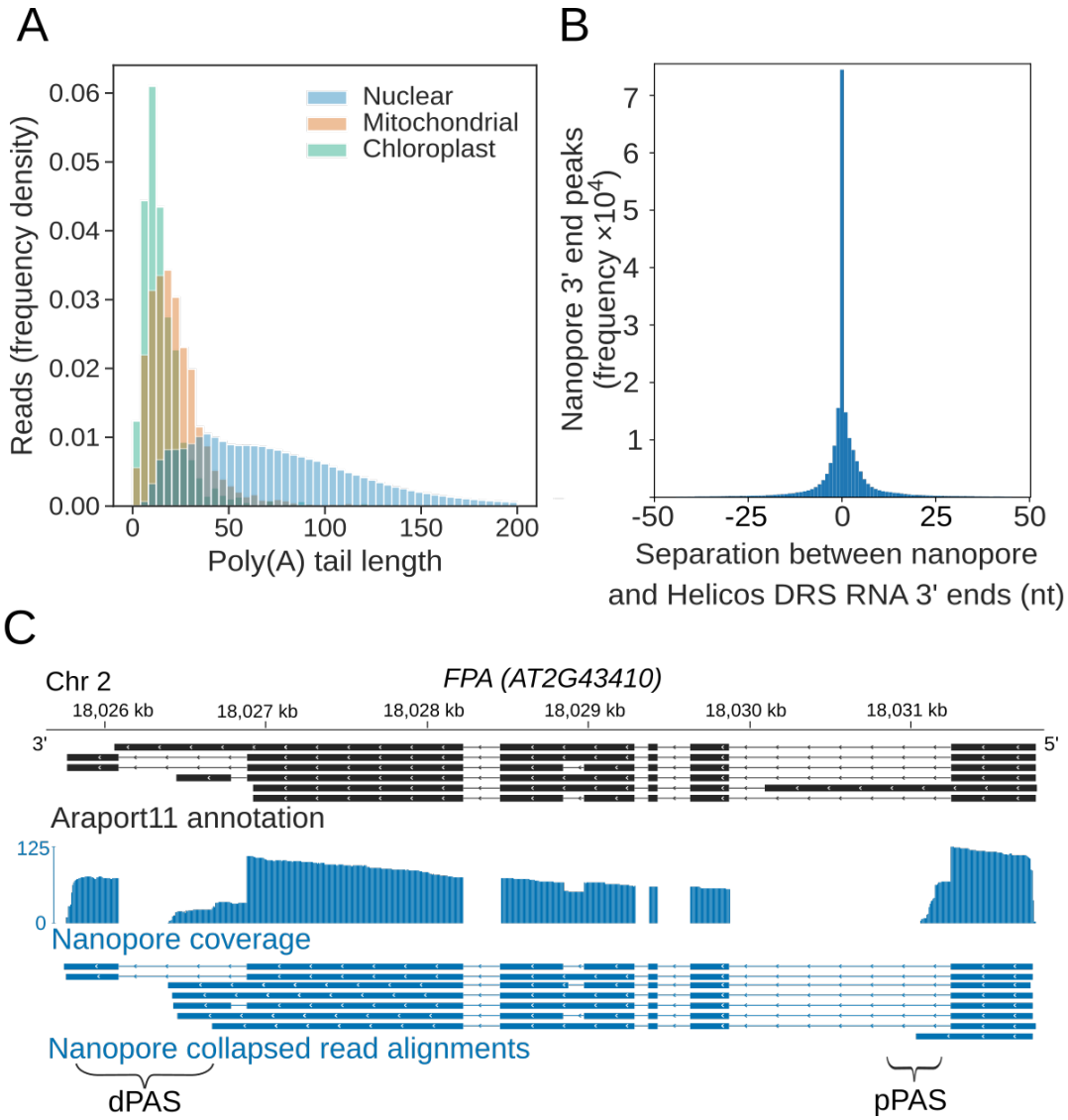

Figure 2. Nanopore DRS reveals poly(A) tail length and maps 3′ cleavage and polyadenylation sites.
(**A**) Normalized histogram showing poly(A) tail length of RNAs encoded by different genomes. Blue, nuclear (n = 2,348,869 reads); orange, mitochondrial (n = 2,490 reads); green, chloroplast (n = 1,848 reads).
(**B**) Distance between the RNA 3′ end positions in nanopore DRS read alignments and the nearest polyadenylation sites identified by Helicos data.
(**C**) Nanopore DRS identified 3′ polyadenylation sites in RNAs transcribed from *FPA (AT2G43410)*. The blue track shows the coverage of nanopore DRS read alignments and collapsed read alignments representing putative transcript annotations detected by nanopore DRS. Black, isoforms found in Araport11 annotation; blue, read alignments from nanopore DRS. pPAS, proximal polyadenylation site; dPAS, distal polyadenylation sites.
[Linked to Supplementary figure 2].

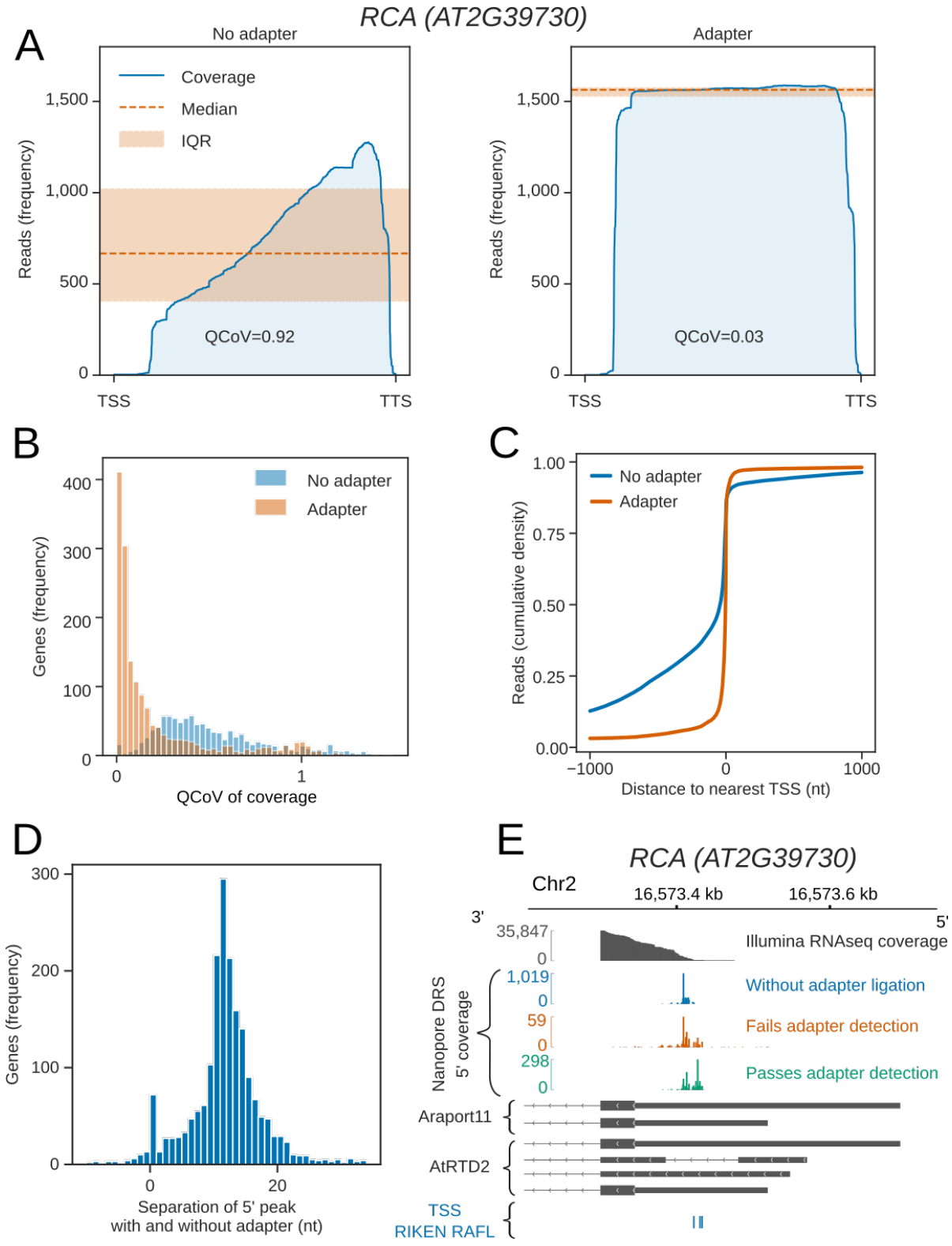

998

999

1000 **Figure 3. Cap-dependent ligation of an adapter enables detection of authentic RNA 5′ ends.**
1001 (**A**) 5′ adapter RNA ligation reduces 3′ bias in nanopore DRS data at *RCA* (*AT2G39730*). Blue line,
1002 exonic read coverage at *RCA* for reads without (left) and with(right) adapter; orange line, median

coverage; orange shaded area, interquartile range (IQR). Change in 3' bias can be measured using the IQR / median = quartile coefficient of variation (QCoV). 5' adapter ligation reduces 3' bias at *RCA* from 0.92 to 0.03.
(**B**) 5' adapter RNA ligation reduces 3' bias in nanopore DRS data. Histogram showing the QCoV in per base coverage for reads with a 5' adapter RNA (orange) compared with reads without a 5' adapter RNA (blue).
(**C**) Cap-dependent adapter ligation allows identification of authentic 5' ends using nanopore DRS. The cumulative distribution function shows the distance to the nearest Transcription Start Site (TSS) identified from full-length transcripts cloned as part of the RIKEN RAFL project for reads with a 5' adapter RNA (orange) compared with reads without a 5' adapter RNA (blue).
(**D**) Cap-dependent adapter ligation enabled resolution of an additional 11 nt of sequence at the RNA 5' end. Histogram showing the nucleotide shift in the largest peak of 5' coverage for each gene in data obtained using protocols with vs without a 5' adapter.
(**E**) For *RCA (AT2G39730),* the 5' end identified using cap-dependent 5' adapter RNA ligation protocol was consistent with Illumina RNAseq and full-length cDNA start site data but differed from the 5' ends in the Araport11 and AtRTD2 annotations. Upper panel: grey, Illumina RNAseq coverage; blue, nanopore DRS 5' end coverage generated without a cap-dependent ligation protocol; green/orange, nanopore DRS 5' end coverage for read alignments generated using the cap-dependent ligation protocol with (green) and without (orange) 5' adapter RNA. Lower panel: grey, RNA isoforms found in Araport11 and AtRTD2 annotations; blue, TSSs identified from full-length transcripts cloned as part of the RIKEN RAFL project.
[Linked to Supplementary figure 3].

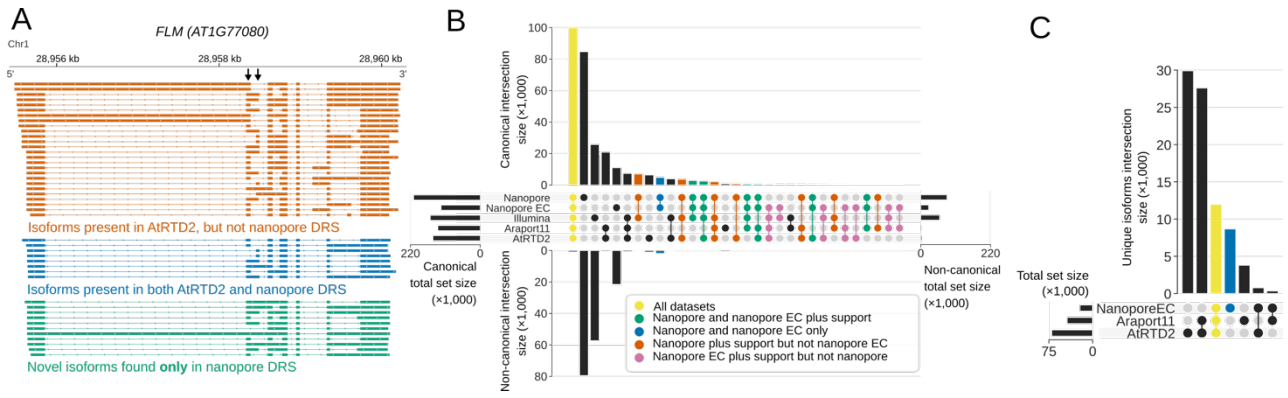

Figure 4. Nanopore DRS reveals the complexity of alternative splicing.

(**A**) Nanopore DRS identified the mutually exclusive alternative splicing of *FLOWERING LOCUS M* (*FLM, AT1G77080)*. Black arrows indicate mutually exclusive exons. Novels isoforms were also identified: orange, isoforms present in the AtRTD2 annotation but not identified using nanopore DRS; blue, isoforms common to both AtRTD2 and nanopore DRS; green, novel isoforms identified in nanopore DRS.

(**B**) Comparison of splicing events identified in error-corrected and non-error-corrected nanopore DRS, Illumina RNA sequencing, and Araport11 and AtRTD2 annotations. Bar size represents the number of unique splicing events common to the set intersection highlighted using circles (see Supplementary table 3 for the exact values). GU/AG splicing events are shown on the top and non-GU/AG on the bottom of the plot: yellow, splicing events common to all five datasets; green, events common to both error-corrected and non-error-corrected nanopore DRS with support in orthogonal datasets; blue, events common to both nanopore DRS datasets without orthogonal support; orange, events found in uncorrected nanopore DRS (but not error corrected) with orthogonal support; pink, events found in error-corrected nanopore DRS (but not uncorrected) with orthogonal support.

(**C**) Comparison of RNA isoforms (defined as sets of co-spliced introns) identified in error-corrected full-length nanopore DRS, Araport11 and AtRTD2 annotations. Bar size represents the number of splicing events common to a group highlighted using circles below (see Supplementary table 3 for the exact values): yellow, unique splicing patterns nanopore DRS and both reference annotations; blue, novel isoforms.

[Linked to Supplementary figure 4].

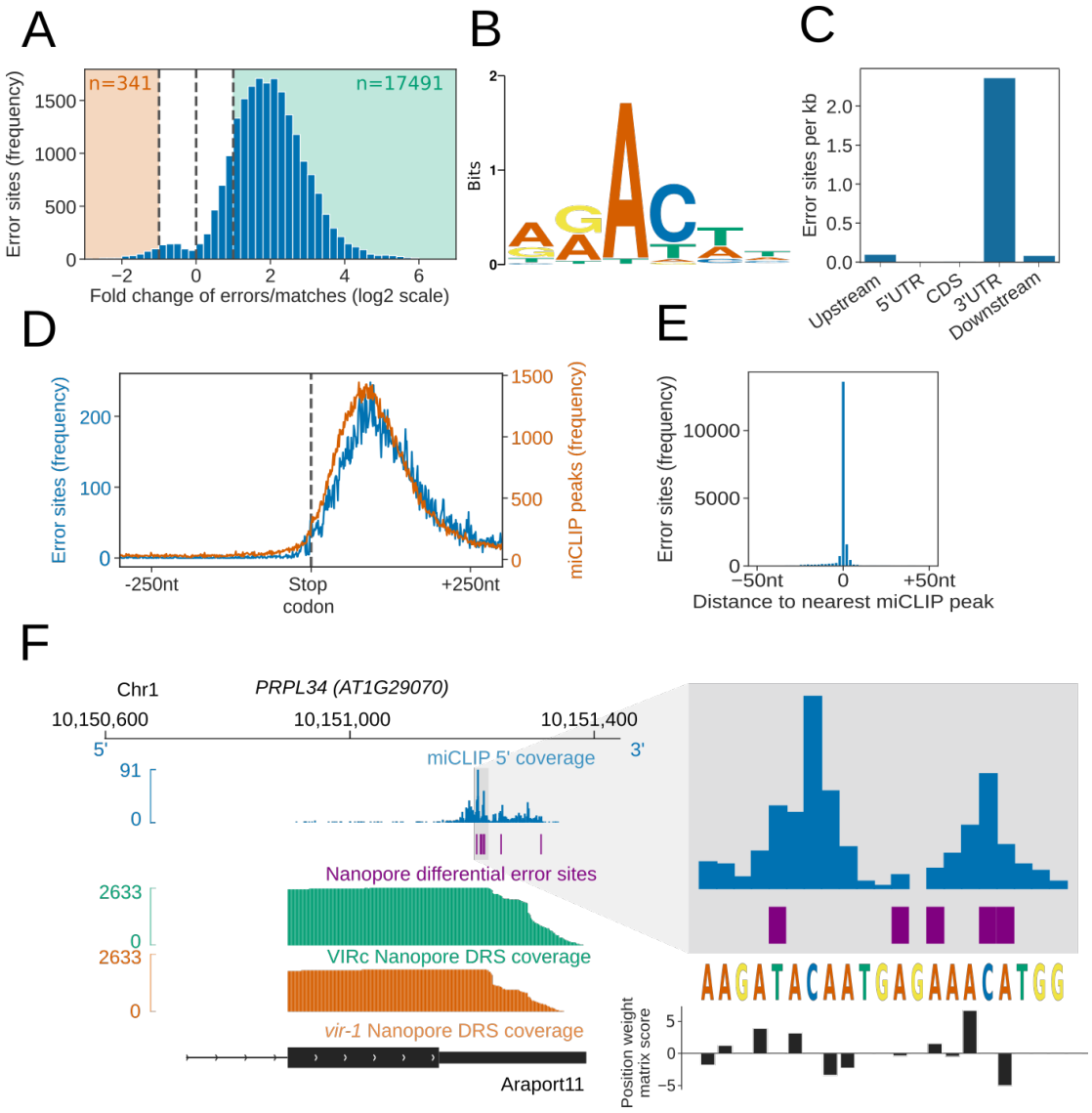

Figure 5. Differential error rate analysis identifies sites of VIR-dependent m^{6}A modifications transcriptome-wide.

(**A**) Loss of VIR function is associated with reduced error rate in nanopore DRS. Histogram showing the log2 fold change in the ratio of errors to reference matches at bases with a significant change in error profile in *vir-1* mutant compared with the VIR-complemented line. Orange and green shaded regions indicate sites with increased and reduced errors in *vir-1,* respectively.

(**B**) The motif at error rate sites matches the consensus m^{6}A target sequence. The sequence logo is for the motif enriched at sites with reduced error rate in the *vir-1* mutant.

(**C**) Differential error rate sites are primarily found in 3' UTRs. Bar plot showing the number of differential error rate sites per kb for different genic feature types of 48,149 protein coding transcript loci in the nuclear genome of the Araport11 reference. Upstream and downstream regions were defined as 200 nt regions 5' and 3' of the annotated transcription termination sites, respectively.

(**D**) Differential error rate sites and miCLIP peaks are similarly distributed within the 3' UTR, without accumulation at the stop codon. Metagene plot centred on stop codons from 48,149 protein coding transcript loci, showing the frequency of nanopore DRS error sites (blue) and miCLIP peaks (orange). (**E**) The locations of differential error rate sites are in good agreement with the locations of miCLIP sites. Histogram showing the distribution of distances to the nearest miCLIP peak for each site of reduced error. Most error sites (77%) are within 5 nt of a miCLIP peak.
(**F**) Nanopore DRS differential error site analysis and miCLIP identify m^6A sites in the 3' UTR of *PRPL34* RNA. Blue, miCLIP 5' end coverage; purple, nanopore DRS differential error sites; green, nanopore DRS coverage of VIR-complemented line (VIRc); orange, nanopore DRS coverage of *vir-1* mutant; black, RNA isoform from Araport11 annotation. The expanded region shows miCLIP coverage (blue) and error sites (purple) scored using the m^6A consensus position weight matrix (black; Figure 5B). A higher positive score denotes a higher likelihood of a match to the consensus sequence.
[Linked to Supplementary figure 5].

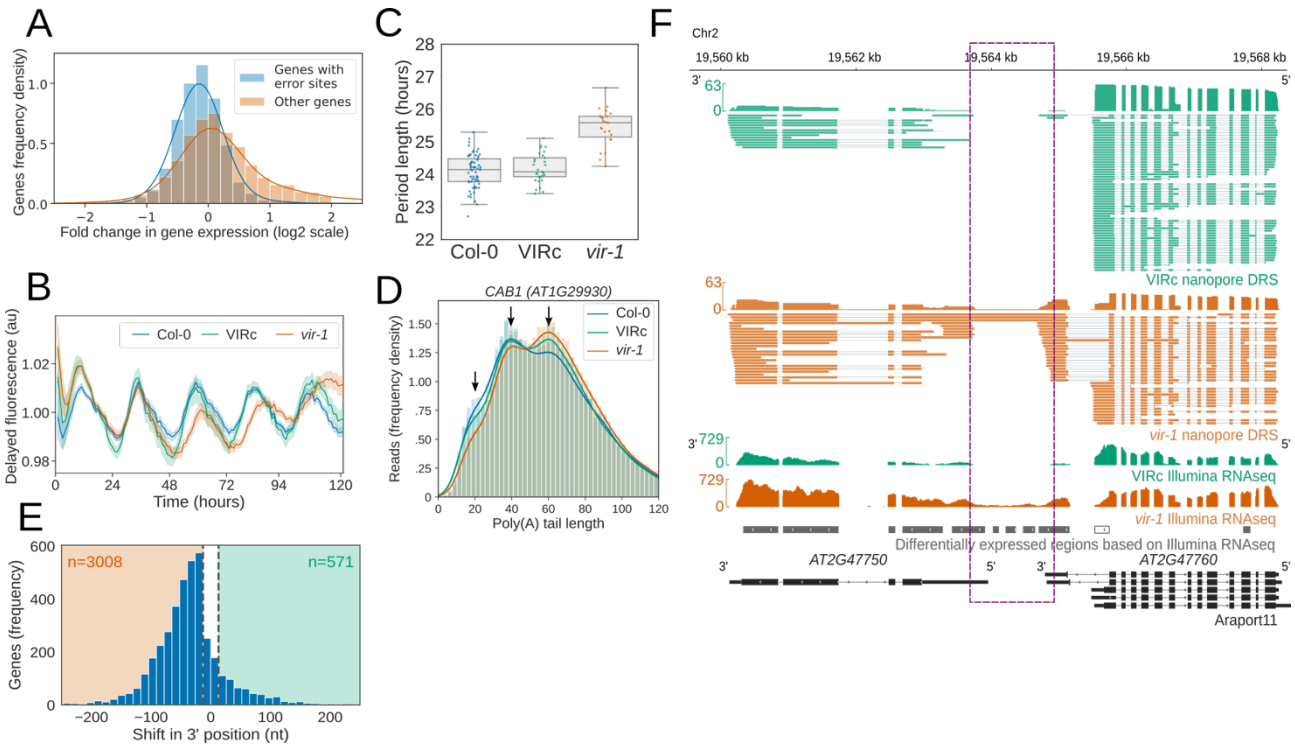

Figure 6. Reduction in m^{6}A RNA modification leads to disruption of the circadian clock and generation of chimeric RNAs.

(**A**) Genes with differential error rate sites have lower detectable RNA levels. Histogram showing the log2 fold change in protein coding gene expression based on counts from nanopore DRS reads in the *vir-1* mutant compared to the VIR-complemented line. Blue, genes with differential error rate sites (n = 5,157 genes); orange, genes with without differential error rate sites (n=14,601 genes).

(**B**) The circadian period is lengthened in the *vir-1* mutant. Mean delayed fluorescence measurements in arbitrary units are shown for Col-0 (blue; n = 61 technical reps), the VIR-complemented line (VIRc; green; n = 29 technical reps) and the *vir-1* mutant (orange; n = 24 technical reps). Shaded areas show bootstrapped 95% confidence intervals for the mean.

(**C**) Boxplot showing the period lengths for Col-0 (blue), VIRc (green) and the *vir-1* mutant (orange), calculated from delayed fluorescence measurements shown in (**B**).

(**D**) Poly(A) tail length is altered in the *vir-1* mutant. Histogram showing the poly(A) tail length distribution of *CAB1 (AT1G29930)* in Col-0 (blue; n=40,841 reads), VIRc (green; n=65,810 reads) and the *vir-1* mutant (orange; n=68,068 reads). Arrows indicate phased peaks of poly(A) length at approximately 20, 40 and 60 nt. *vir-1* distribution is significantly different from both Col-0 and VIRc, according to the Kolmogorov–Smirnov test (p=1.3×10^{-76}, p=4.7×10^{-49} respectively).

(**E**) Global change in 3′ end usage in the *vir-1* mutant compared with the VIRc line. Histogram showing the distance in nucleotides between the most reduced and most increased 3′ end positions for genes in which the 3′ end profile is altered in *vir-1* (detected with the Kolmogorov–Smirnov test, FDR < 0.05). A threshold of 13 nt was used to detect changes in the 3′ end position.

(**F**) Readthough events and chimeric RNAs are detected in *vir-1*. Green, nanopore DRS and Illumina RNAseq data for the VIRc line; orange, nanopore DRS and Illumina RNAseq data for the *vir-1* mutant;

1110 black, RNA isoforms found in Araport11 annotation. Differentially expressed regions between *vir-1*
1111 and VIRc detected using Illumina RNAseq data with DERfinder are shown in grey (for upregulated
1112 regions) or white (for downregulated regions). Intergenic readthrough regions are highlighted by the
1113 purple dashed rectangle.
1114 **[Linked to Supplementary figure 6].**
1115
1116

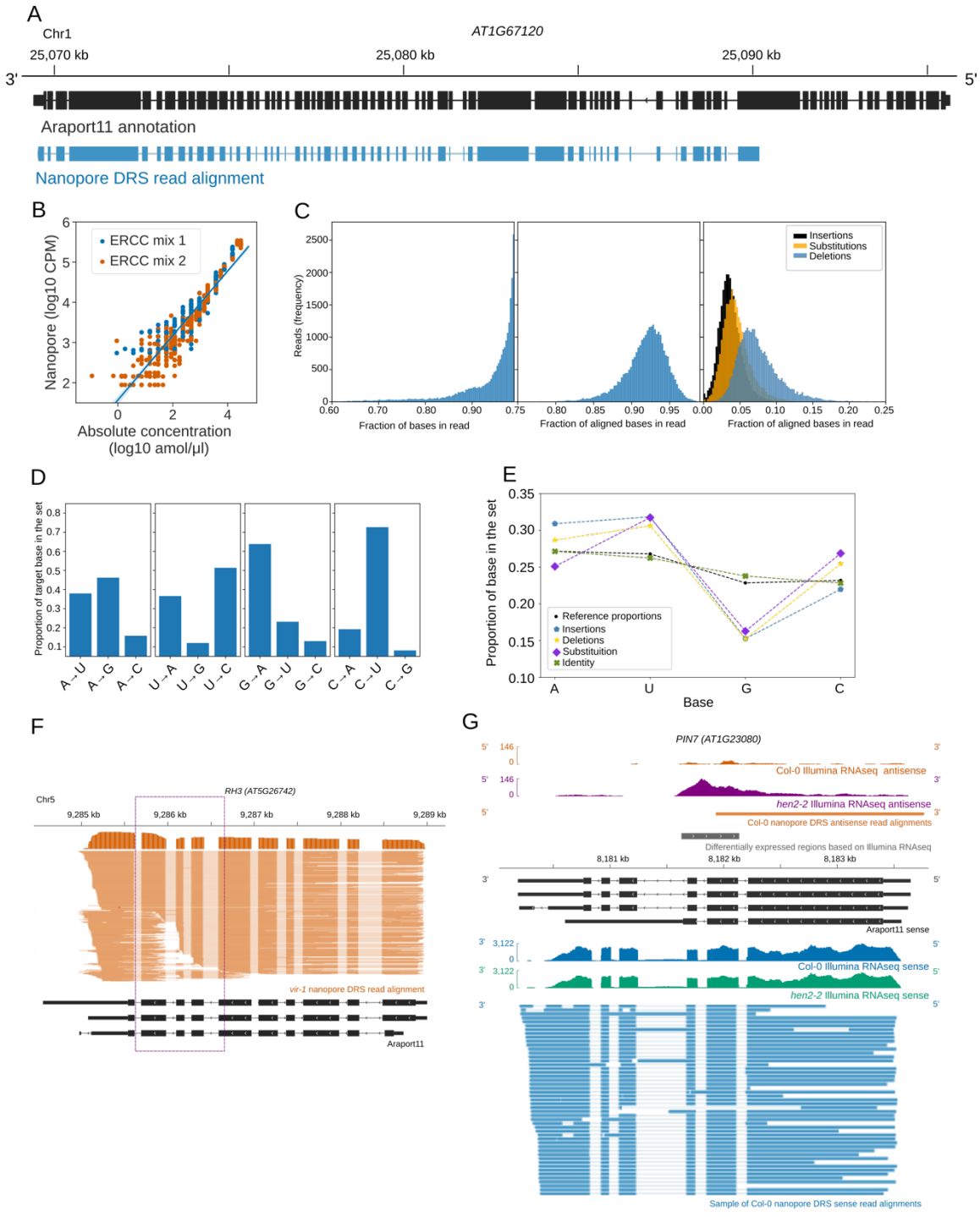

Supplementary figure 1. Properties of nanopore DRS sequencing data.

(**A**) Nanopore DRS identified a 12.8 kb transcript generated from the *AT1G67120* gene that includes 58 exons. Black, RNA isoform present in the Araport11 annotation; blue, an RNA isoform identified using nanopore DRS.

(**B**) Synthetic ERCC RNA Spike-In mixes are detected in a quantitative manner. Absolute concentrations of spike-ins are plotted against counts per million (CPM) reads in log10 scale. Blue, ERCC RNA Spike-In mix 1; orange, ERCC RNA Spike-In mix 2.
(**C**) Overview of the sequencing and alignment characteristics of nanopore DRS data for ERCC RNA Spike-Ins. Left, distribution of the length fraction of each sequenced read that aligns to the ERCC RNA Spike-In reference; centre, distribution of fraction of identity that matches between the sequence of the read and the ERCC RNA Spike-In reference for the aligned portion of each read; right, distributions of the occurrence of insertions (black), substitutions (orange) and deletions (blue) as a proportion of the number of aligned bases in each read.
(**D**) Substitution preference for each nucleotide (left to right: adenine [A], uracil [U], guanine [G], cytosine [C]). When substituted, G is replaced with A in more than 63% of its substitutions, while C is replaced by U in 73%. Conversely, U is rarely replaced with G (12%) and A is rarely substituted with C (16%).
(**E**) Nucleotide representation within the ERCC RNA Spike-In reference sequences (black dots) compared with nucleotide representation within four categories from the nanopore DRS reads. Identity matches between the sequence of the read and the ERCC RNA Spike-In reference (green crosses), insertions (blue pentagons), deletions (yellow stars) and substitutions (purple diamonds).G is under-represented and U is over-represented for all three categories of error (insertion, deletion and substitution) relative to the reference nucleotide distribution. C is over-represented in deletions and substitutions. A is over-represented in insertions and deletions and under-represented in substitutions.
(**F**) Signals originating from the *RH3* transcripts are susceptible to systematic over-splitting around exons 7–9 (highlighted using a purple dashed box), resulting in reads with apparently novel 5′ or 3′ positions. This appears only to occur at high frequency in datasets collected after May 2018 (Supplementary table 1) and may result from an update to the MinKNOW software.
(**G**) *PIN7* long non-coding antisense RNAs detected using nanopore DRS. Blue, Col-0 sense Illumina RNAseq coverage and nanopore sense read alignments; orange, Col-0 antisense Illumina RNAseq coverage and nanopore antisense read alignments; green, *hen2–2* mutant sense Illumina RNAseq coverage; purple, *hen2–2* mutant antisense Illumina RNAseq coverage; black, sense RNA isoforms found in Araport11 annotation; grey, antisense differentially expressed regions detected with DERfinder.
[Linked to Figure 1]

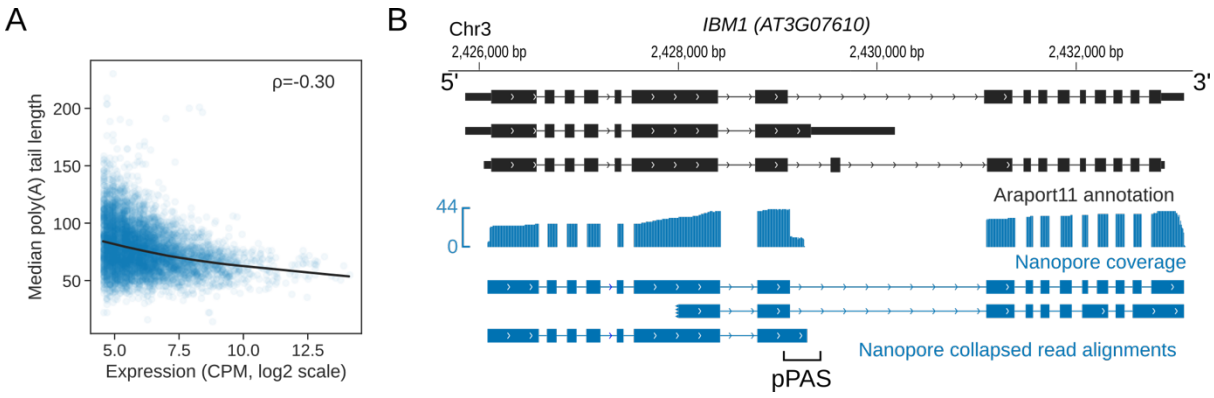

Supplementary figure 2. 3′ end processing is revealed by nanopore DRS.

(**A**) The RNA poly(A) tail length negatively correlates with the gene expression level. Expression in log2 scale of counts per million (CPM) obtained from nanopore DRS data is plotted against the median poly(A) tail length. ρ, Spearman's correlation coefficient; black line, locally weighted scatterplot smoothing (LOWESS) regression fit.

(**B**) Nanopore DRS identified 3′ polyadenylation sites in RNAs transcribed from the *IBM1 (AT3G07610)* gene. The blue track shows the coverage of nanopore DRS reads. Black, isoforms found in Araport11 annotation; blue, isoforms those detected by nanopore DRS. pPAS, proximal polyadenylation site.

[Linked to Figure 2].

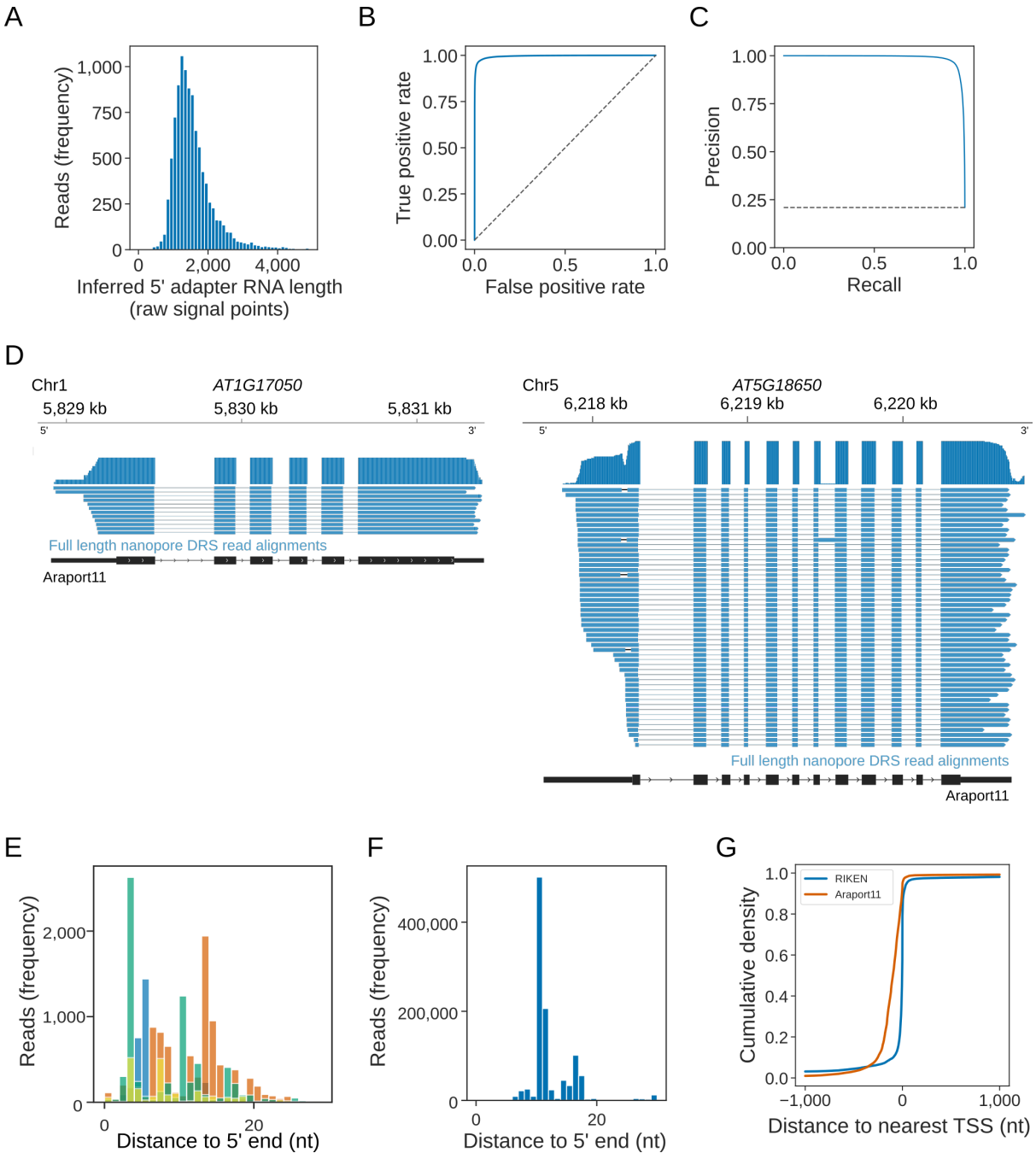

Supplementary figure 3. Nanopore DRS with cap-dependent ligation of 5′ adapter RNA.
(**A**) Histogram showing the distribution of 5′ adapter RNA length in the nanopore raw current signal, as inferred from alignment of the mRNA sequence to the signal using nanopolish eventalign. The median signal length was 1,441 points and 96% of adapter signals were 3,000 points or less.
(**B**) Out-of-bag receiver operator characteristic curve showing the performance of the trained convolutional neural network at detecting 5′ adapter RNA using 3,000 points of signal. The curve was generated using five-fold cross validation.
(**C**) Out-of-bag precision recall curve showing the performance of trained neural network, generated using five-fold cross validation.

(**D**) Alternative transcription start sites were identified using nanopore DRS with cap-dependent ligation of a 5′ end adapter at the *AT1G17050* and *AT5G18650* genes. The blue track shows the coverage of nanopore DRS reads. Black, isoforms found in the Araport11 annotation; blue, isoforms detected by nanopore DRS with cap-dependent ligation of 5′ adapter RNA.
(**E**) Reads mapping to ERCC RNA Spike-Ins lack approximately 11 nt of sequence at the 5′ end. Histogram showing the distance to the 5′ end for ERCC RNA Spike-In reads (each spike-in is shown in a different colour; only those with >1,000 supporting reads are shown).
(**F**) Reads mapping to *in vitro* transcribed mGFP lack approximately 11 nt of sequence at the 5′ end. Histogram showing the distance to the 5′ end for *in vitro* transcribed mGFP.
(**G**) Araport11 annotation overestimates the length of 5′ UTRs. The cumulative distribution function shows the distance to the nearest TSS identified from full-length transcripts cloned as part of the RIKEN RAFL project (blue) and Araport11 annotation (orange).
[Linked to Figure 3].

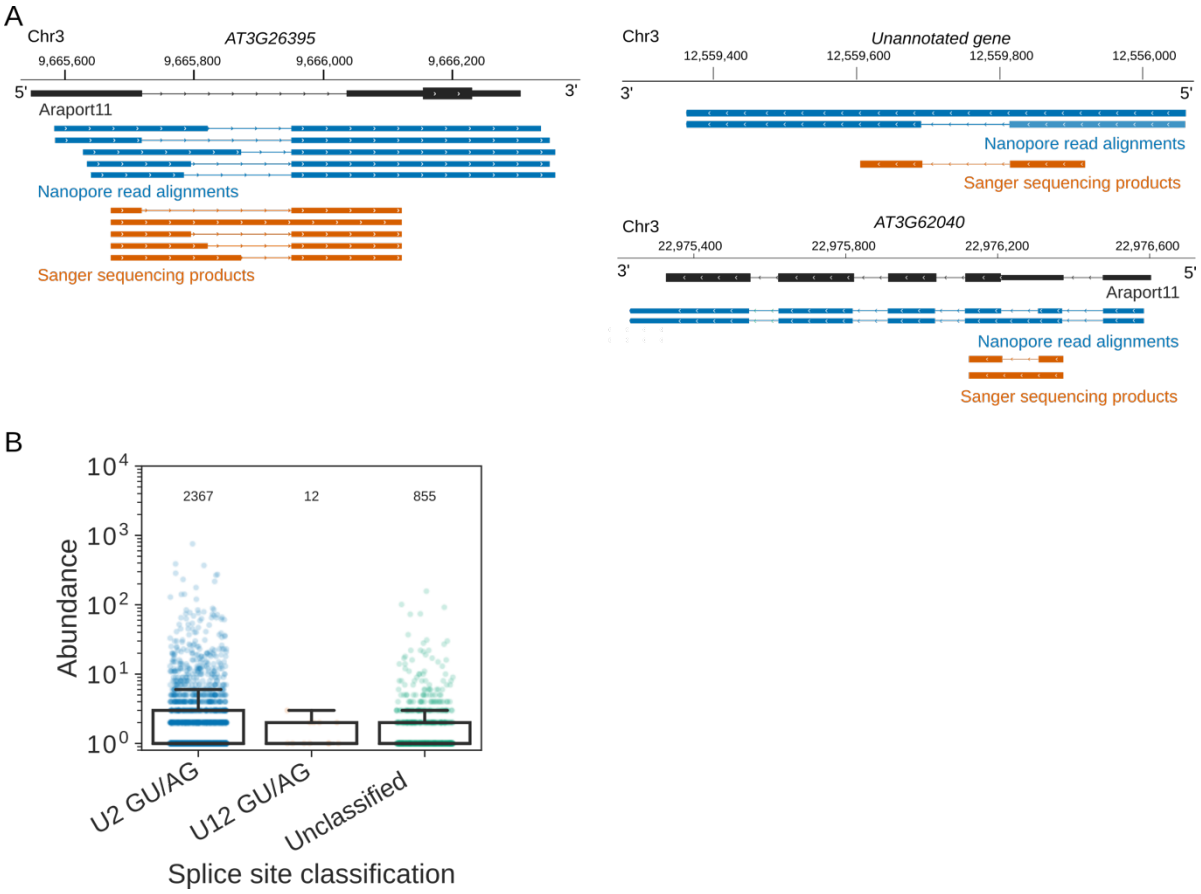

Supplementary figure 4. Patterns of splicing revealed using nanopore DRS.
(**A**) Nanopore DRS can be validated using RT-PCR. Five of the top 20 most highly expressed RNAs with novel splice sites were selected; of these, three were validated by RT-PCR followed by Sanger sequencing of the DNA products. Black, RNA isoforms present in the Araport11 annotation; blue, RNA isoforms found using nanopore DRS; orange, Sanger sequencing products obtained using RT-PCR.
(**B**) Splice junction classification of unannotated GU/AG splice sites found in error-corrected nanopore DRS data that also have Illumina support. Counts are plotted in log10 scale and the exact number of splice junctions in each set is indicated.
[Linked to Figure 4].

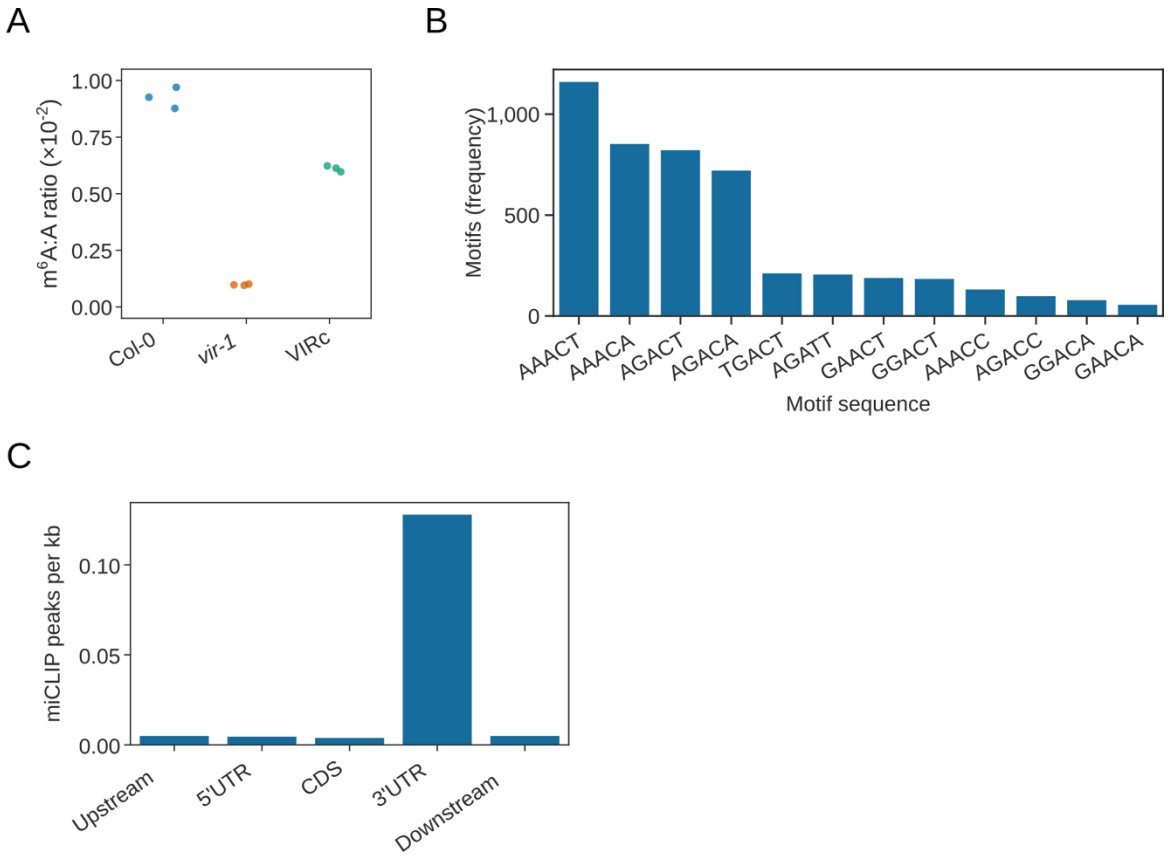

Supplementary figure 5. Identification of VIR-dependent m^{6}A transcriptome-wide.

(**A**) *vir-1* shows reduced levels of m^{6}A compared with Col-0 and restored m^{6}A levels in the VIR-complemented line (VIRc)**.** The ratio of m^{6}A/A obtained using LC-MS analysis is shown Col-0 (blue), *vir-1* (orange) and VIRc (green).

(**B**) Frequency of m^{6}A motifs detected at *vir-1* reduced error sites, as detected by FIMO using the motif detected *de novo* by MEME and an FDR threshold of 0.1.

(**C**) Bar plot showing the number of miCLIP peaks per kb of different genic feature types in the Araport11 reference. Upstream and downstream regions were defined as 200 nt regions before and after the annotated transcription termination sites, respectively.

[Linked to Figure 5].

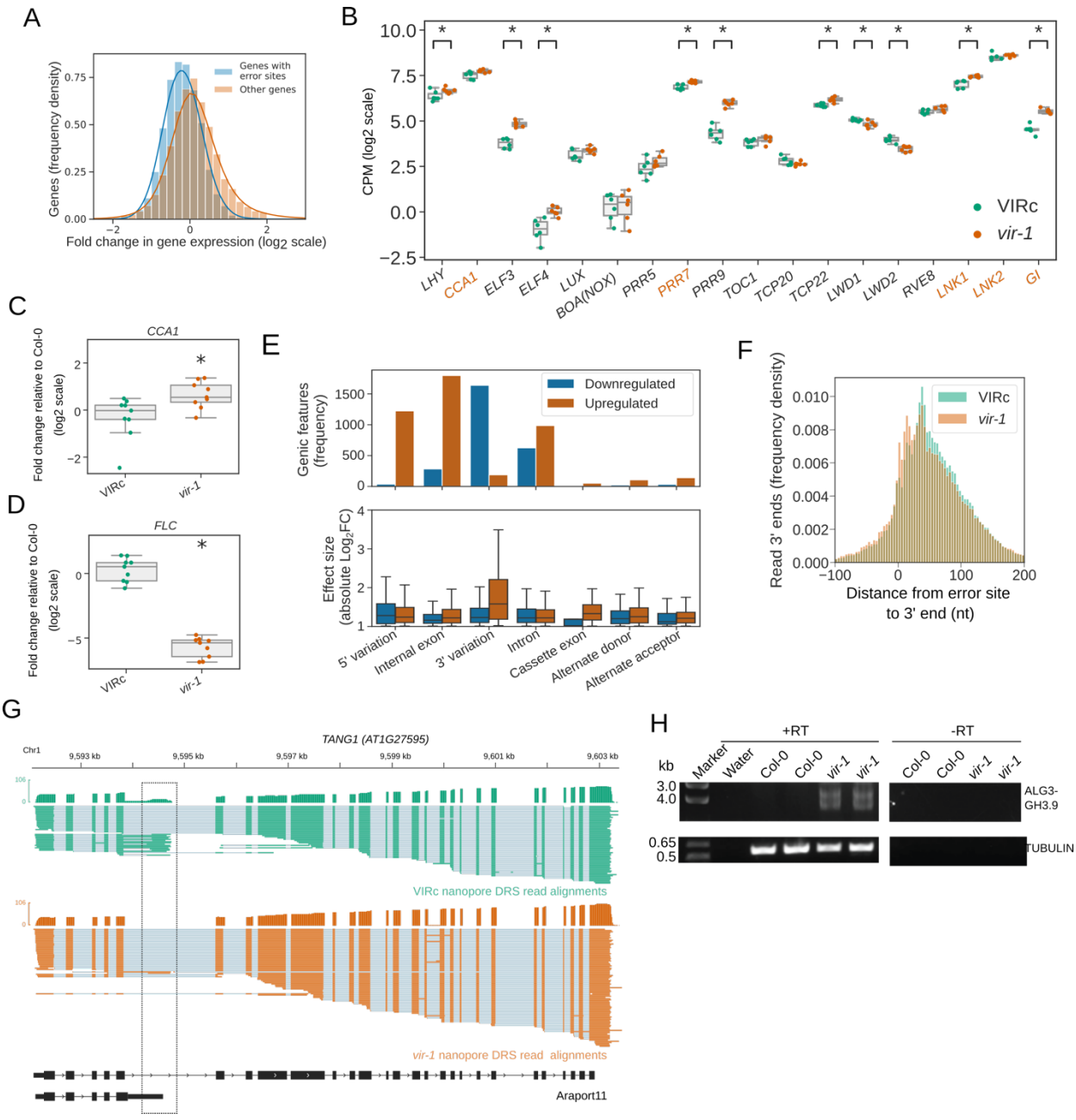

Supplementary figure 6. Changes in the gene expression of circadian clock components and in RNA 3' end formation in the *vir-1* mutant.

(**A**) Histogram showing log2 fold changes in gene expression based on Illumina RNAseq data for the *vir-1* mutant and VIR-complemented line. Blue, genes with differential error rate sites (n=5,169 genes); orange, genes without differential error rate sites (n=14,612 genes).

(**B**) Expression of core circadian clock components is perturbed in the *vir-1* mutant. Boxplots showing normalized gene expression measured using Illumina RNAseq in log2 counts per million (CPM): green, the VIR-complemented line (VIRc); orange, the *vir-1* mutant. Each scatter point represents a single biological replicate. Asterisks denote significant expression changes (using an FDR threshold of 0.05). Orange labelled genes have 3' UTR m^6A detectable by nanopore DRS and miCLIP.

(**C**) Expression of *CCA1*, encoding a regulator of the circadian rhythm in Arabidopsis, is increased in the *vir-1* mutant. Boxplot showing the gene expression change from Col-0 (measured by RT-qPCR)

for VIRc (green) and *vir-1* (orange). Three technical replicates of three biological replicates were conducted. Each scatter point represents the comparison of a technical replicate of treatment (VIRc or *vir-1*) against control (Col-0). The expression change in *vir-1* is significant (p=0.02).
(**D**) Expression of the *Flowering Locus C* (*FLC*) gene is decreased in the *vir-1* mutant. Boxplot showing gene expression change from Col-0 (measured by RT-qPCR) for VIRc (green) and *vir-1* (orange). Three technical replicates of three biological replicates were conducted. Each scatter point represents the comparison of a technical replicate of treatment (VIRc or *vir-1*) against control (Col-0). Expression change in *vir-1* is significant (p=2.4×10^{-14}).
(**E**) Splicing is moderately disrupted in the *vir-1* mutant. Results of differential exon usage analysis with DEXseq are shown for contiguous regions ("exon chunks"), which occur in the same sets of transcripts in the Araport11 reference. Regions were classified as a 5' or 3' variation if they were bounded by the TSS of one or more transcripts. Orange, features with increased usage; blue, features with reduced usage. Boxplots show the distribution in absolute log2 fold change for each feature set.
(**F**) A shift to the use of more proximal polyadenylation sites is observed in m^{6}A containing transcripts in the *vir-1* mutant. Histogram showing distance from the error site (n=17,491 error sites) to upstream and downstream 3' ends in the *vir-1* mutant (orange) and VIRc (green).
(**G**) *vir-1* mutants exhibit increased readthrough of an intronic proximal poly(A) site in intron 5 of the Symplekin domain encoding gene *TANG1*. green, nanopore DRS reads from VIRc; orange, nanopore DRS reads from the *vir-1* mutant; black, Araport11 annotation. The dashed black box highlights the site of proximal polyadenylation.
(**H**) *ALG3-GH3.9* chimeric RNAs are generated in the *vir-1* mutant. RT-PCR gel showing formation of chimeric RNAs in the *vir-1* mutant compared with Col-0.
[Linked to Figure 6].

Sequencing date	Genotype	Bio replicate	5' Adapter ligation	Total reads basecalled	Reads mapped to ERCC spike-ins	Reads mapped to TAIR10	Longest read mapped to ERCC spike-ins	Median length of reads mapped to ERCC spike-ins	Longest read mapped to TAIR10	Median length of reads mapped to TAIR10	Percentage mapped to TAIR10	Estimated over-splitting rate (%)
01/02/2018	Col-0	1	-	1,647,484	6756	1,003,137	1,905	481	12,607	865	60.89	0.047
27/02/2018	vir-1	1	-	1,431,457	1074	1,005,664	2,304	492	12,446	878	70.25	0.045
01/03/2018	VIRc	1	-	1,393,351	713	1,101,368	1,108	493	11,994	873	79.04	0.111
05/04/2018	Col-0	2	-	966,529	556	743,684	1,099	492	11,852	878	76.94	0.035
11/04/2018	Col-0	1	+	1,365,809	7005	345,799	1,928	486	5,663	737	25.32	0.047
13/04/2018	Col-0	2	-	1,242,616	701	930,629	1,094	488	11,434	858	74.89	0.040
16/04/2018	Col-0	3	-	1,079,578	907	757,028	1,772	486	12,744	840	70.12	0.019
18/04/2018	Col-0	4	-	1,007,278	525	765,322	1,292	495	11,542	840	75.98	0.019
08/05/2018	Col-0	2	+	2,043,751	11324	557,949	2,308	507	5,596	732	27.30	0.069
07/09/2018	VIRc	2	-	1,699,123	1824	1,538,040	2,236	497	12,015	871	90.52	0.809
12/09/2018	vir-1	2	-	858,747	1094	812,517	1,880	491	15,040	846	94.62	0.959
25/09/2018	VIRc	4	-	1,435,808	2710	1,318,857	1,947	493	10,836	832	91.85	1.600
28/09/2018	vir-1	3	-	1,843,192	865	1,746,153	1,134	480	15,291	884	94.74	0.878
03/10/2018	vir-1	4	-	1,355,795	1436	1,271,511	1,128	487	11,522	802	93.78	1.467
19/10/2018	VIRc	3	-	1,678,723	1548	1,570,040	2,127	500	11,471	849	93.53	0.887

1259

Supplementary table 1. Properties of the nanopore DRS sequencing data.
Dataset statistics for all nanopore DRS sequencing runs conducted. Datasets are sorted by the date of the sequencing run. All data was collected using a MinION with R9.4 flow cell and SQK-RNA001 library kit. Increases in mapping and over-splitting rate that occur in samples collected after September 2018 are therefore likely to have resulted from changes in the MinKNOW software. **[Linked to Figure 1 through 6].**

A

Replicate 1	Adapter		No adapter		Signal-to-noise ratio
	Fails	Passes	Fails	Passes	
Match length > 10 nt	58,078	211,786	47,548	11,427	15.17
Log_{10} E value < 2	76,926	192,938	57,874	1,101	131.8
Adapter matches directly after alignment	198,296	71,568	58,936	39	545.4

B

Replicate 2	Adapter		No adapter		Signal-to-noise ratio
	Fails	Passes	Fails	Passes	
Match length > 10 nt	37,631	342,158	100,791	12,653	72.4
Log_{10} E value < 2	60,605	319,184	112,781	663	895.9
Adapter matches directly after alignment	266,812	112,977	113,429	15	3,202

Supplementary table 2. Adapter detection using BLASTN rules approach.
The number of reads with adapters were detected in two biological replicates (Tables A and B respectively) of Col-0 sequenced with and without adapter ligation protocol. Rules are applied cumulatively (i.e. row one shows reads that pass the first rule, row two shows reads that pass the first and second rules, etc.). The signal-to-noise ratio shows the number of positive examples detected using rules in the adapter-ligated dataset divided by the number of false positives from the dataset collected without adapters.
[Linked to Figure 3].

1280 **A**

AtRTD2	Araport11	Illumina	Nanopore EC	Nanopore	Canonical	Non-canonical
■	■	■	■	■	99,966	805
				■	84,630	79,377
		■			25,769	57,298
■	■				20,893	404
			■		10,882	21,484
■	■	■			7,301	545
		■		■	6,941	210
■					6,256	879
			■	■	4,801	1,894
■		■			3,939	160
■		■		■	3,665	31
		■	■	■	2,844	59
■		■	■	■	2,424	28
■	■	■		■	2,006	18
	■				832	453
■				■	828	5
	■	■	■	■	585	6
■	■		■	■	512	6
■	■	■	■		484	31
		■	■		390	53
	■	■			369	33
■	■			■	326	2

■			■	■	193	6
■		■	■		148	8
	■	■		■	76	3
■	■		■		47	4
■			■		24	0
	■		■	■	21	0
	■			■	20	0
	■	■	■		18	0
	■		■		1	0

B

atRTD2	Araport11	DRS EC	Isoforms
■			29,894
■	■		27,585
■	■	■	11,967
		■	8,659
	■		3,788
■		■	756
	■	■	341

Supplementary table 3. Splice junctions supported by nanopore DRS and Illumina RNAseq.
Numbers are shown for (A) the unique splice junction set intersections upset plot (Figure 4B) and (B) unique linked splicing events upset plot (Figure 4C). Shaded cells denote sets included in the intersection for that row, while unshaded cells denote sets excluded from the intersection. Rows are sorted by the size of the intersection for canonical splice junctions.
[Linked to Figure 4].

1291

AGI locus ID	Gene name	Pathway	log2 fold change	Log2 counts per million	False discovery Rate	Differentially expressed (abs logFC > 1, FDR < 0.05)
AT2G19520	FVE	Autonomous	-0.40	5.49	3.95E-08	-
AT2G21660	ATGRP7	Autonomous	0.03	6.11	8.57E-01	-
AT2G43410	FPA	Autonomous	0.70	5.03	1.75E-11	-
AT3G04610	FLK	Autonomous	0.29	5.18	5.90E-04	-
AT3G10390	FLD	Autonomous	0.31	3.80	6.68E-03	-
AT4G02560	LD	Autonomous	0.68	4.36	7.49E-09	-
AT4G16280	FCA	Autonomous	0.71	5.02	2.90E-09	-
AT5G13480	FY	Autonomous	0.49	3.80	8.78E-04	-
AT4G22950	AGL19	FLC-independent vernalization pathway	1.10	0.81	9.17E-04	+
AT2G45660	SOC1	Floral integrator	-1.64	6.72	4.55E-84	+
AT5G60910	FUL	Floral integrator and flower meristem identity	-1.13	2.09	1.84E-09	+
AT1G25560	TEM1	Floral repressor	-0.81	6.50	3.83E-02	-
AT1G68840	TEM2	Floral repressor	-0.19	7.08	6.30E-01	-
AT2G22540	SVP	Floral repressor	-0.29	6.96	2.20E-03	-
AT3G57390	AGL18	Floral repressor	0.10	3.30	5.36E-01	-
AT5G13790	AGL15	Floral repressor	0.52	1.02	7.22E-02	-
AT1G24260	SEP3	Flower development	1.02	2.82	9.91E-09	+
AT1G02400	GA2ox6	Gibberellin	0.43	2.09	3.69E-02	-
AT1G14920	GAI	Gibberellin	-0.27	6.22	5.95E-03	-
AT1G15550	GA3ox1	Gibberellin	-0.68	1.36	1.72E-02	-
AT1G18075	miR159b	Gibberellin	0.72	0.13	4.98E-02	-
AT1G30040	GA2ox2	Gibberellin	-0.08	1.86	8.15E-01	-
AT1G47990	GA2ox4	Gibberellin	-0.12	0.76	7.18E-01	-
AT1G78440	GA2ox1	Gibberellin	-1.43	-0.19	2.57E-04	+
AT1G79460	GA2	Gibberellin	-0.33	2.80	4.69E-02	-
AT2G01570	RGA	Gibberellin	-0.09	7.22	4.01E-01	-
AT3G05120	GID1A	Gibberellin	-0.33	4.93	1.74E-03	-
AT3G11440	MYB65	Gibberellin	-0.37	1.99	4.23E-02	-
AT3G63010	GID1B	Gibberellin	0.76	3.51	4.26E-12	-
AT4G02780	CPS1	Gibberellin	0.68	0.33	2.28E-02	-
AT4G24210	SLY1	Gibberellin	-0.39	4.02	2.31E-03	-
AT4G25420	GA20ox1	Gibberellin	0.18	1.48	5.58E-01	-
AT5G06100	MYB33	Gibberellin	0.17	3.76	1.20E-01	-
AT5G27320	GID1C	Gibberellin	-0.06	4.74	6.60E-01	-
AT5G51810	GA20ox2	Gibberellin	-1.75	1.94	7.84E-14	+
AT5G03840	TFL1	Inflorescence architecture	-1.68	-0.43	1.64E-05	+
AT2G27990	PNF	Inflorescence meristem development	0.52	1.78	1.60E-03	-
AT5G02030	PNY	Inflorescence meristem development	0.08	4.08	5.24E-01	-
AT1G04400	CRY2	Light perception	-0.28	7.25	4.69E-03	-
AT1G09570	PHYA	Light perception	0.01	7.56	9.35E-01	-
AT2G18790	PHYB	Light perception	0.13	6.35	2.45E-01	-
AT1G25540	PFT1	Light perception	0.28	4.49	9.86E-03	-
AT4G34530	CIB1	Light signalling	-0.99	4.14	2.13E-04	-
AT5G46210	CUL4	Light signalling	0.14	6.54	7.76E-02	-
AT4G24540	AGL24	Meristem response	-1.14	2.49	1.99E-08	+
AT4G35900	FD	Meristem response	-0.31	1.78	2.46E-01	-
AT1G53090	SPA4	Photoperiod	0.17	4.96	6.88E-02	-
AT1G65480	FT	Photoperiod	-1.75	-0.32	6.10E-08	+
AT1G69570	CDF5	Photoperiod	-0.34	4.05	7.97E-02	-
AT2G28550	TOE1	Photoperiod	0.94	6.42	1.16E-24	-
AT2G32950	COP1	Photoperiod	0.53	5.43	5.84E-09	-
AT2G34720	NFYA4	Photoperiod	-0.31	5.45	7.93E-03	-
AT2G38880	NFYB1	Photoperiod	-0.44	3.93	8.79E-06	-
AT2G39250	SNZ	Photoperiod	0.65	4.99	2.46E-09	-
AT2G46340	SPA1	Photoperiod	0.58	7.45	4.89E-11	-
AT2G47700	RFI2	Photoperiod	-0.44	5.55	3.52E-05	-
AT3G15354	SPA3	Photoperiod	0.84	6.06	1.01E-13	-
AT3G47500	CDF3	Photoperiod	0.62	6.44	8.79E-11	-
AT3G48590	NFYC1	Photoperiod	-0.67	4.61	2.85E-09	-
AT3G54990	SMZ	Photoperiod	0.54	2.37	1.39E-02	-
AT4G11110	SPA2	Photoperiod	0.28	5.26	2.56E-03	-
AT4G14540	NFYB3	Photoperiod	0.23	5.21	1.93E-02	-
AT5G12840	NFYA1	Photoperiod	-0.30	5.15	2.97E-04	-

AT5G39660	CDF2	Photoperiod	-0.25	5.03	1.65E-01	-
AT5G47640	NFYB2	Photoperiod	-0.30	6.06	2.59E-03	-
AT5G57660	COL5	Photoperiod	-0.67	8.85	7.86E-07	-
AT5G60120	TOE2	photoperiod	0.38	4.71	6.29E-05	-
AT5G62430	CDF1	Photoperiod	-0.01	5.50	9.25E-01	-
AT3G22380	TIC	Photoperiod, circadian clock	0.68	8.16	5.64E-15	-
AT5G57360	ZTL	Photoperiod, circadian clock	0.18	6.13	3.36E-02	-
AT1G01060	LHY	Photoperiod, circadian clock	0.32	6.54	1.85E-02	-
AT1G09530	PIF3	Photoperiod, circadian clock	-0.31	4.76	4.49E-02	-
AT1G12910	LWD1	Photoperiod, circadian clock	-0.29	4.94	3.13E-03	-
AT1G22770	GI	Photoperiod, circadian clock	0.93	5.13	3.98E-16	-
AT2G18915	LKP2	Photoperiod, circadian clock	-0.38	4.47	2.23E-03	-
AT2G21070	FIO1	Photoperiod, circadian clock	0.31	2.93	1.67E-02	-
AT2G25930	ELF3	Photoperiod, circadian clock	0.99	4.41	1.04E-14	-
AT2G40080	ELF4	Photoperiod, circadian clock	1.01	-0.36	2.20E-03	+
AT2G46790	PRR9	Photoperiod, circadian clock	1.55	5.39	3.77E-20	+
AT2G46830	CCA1	Photoperiod, circadian clock	0.04	7.64	7.18E-01	-
AT3G04910	WNK1	Photoperiod, circadian clock	-0.41	7.16	2.29E-04	-
AT3G26640	LWD2	Photoperiod, circadian clock	-0.57	3.75	1.89E-06	-
AT3G46640	LUX	Photoperiod, circadian clock	0.26	3.28	1.86E-01	-
AT3G60250	CKB3	Photoperiod, circadian clock	-0.53	5.49	3.48E-06	-
AT4G08920	CRY1	Photoperiod, circadian clock	-0.36	8.36	5.54E-05	-
AT4G16250	PHYD	Photoperiod, circadian clock	1.14	4.13	1.97E-19	+
AT4G18130	PHYE	Photoperiod, circadian clock	0.77	5.50	1.49E-14	-
AT5G02810	PRR7	Photoperiod, circadian clock	0.23	7.01	5.61E-03	-
AT5G08330	CHE	Photoperiod, circadian clock	-0.86	6.21	8.99E-11	-
AT5G24470	PRR5	Photoperiod, circadian clock	0.31	2.67	2.29E-01	-
AT5G35840	PHYC	Photoperiod, circadian clock	0.46	5.53	2.50E-06	-
AT5G37260	CIR1	Photoperiod, circadian clock	0.25	3.12	1.60E-01	-
AT5G59560	SRR1	Photoperiod, circadian clock	-0.28	3.43	4.74E-02	-
AT5G60100	PRR3	Photoperiod, circadian clock	1.69	0.92	5.93E-11	+
AT5G61380	PRR1	Photoperiod, circadian clock	0.12	3.91	3.92E-01	-
AT5G64813	LIP1	Photoperiod, circadian clock	-0.33	4.75	5.34E-04	-
AT1G68050	FKF1	Photoperiod, circadian clock	0.68	-0.32	3.91E-02	-
AT5G17690	TFL2	Photoperiod, vernalization and flower development	0.00	4.46	9.97E-01	-
AT2G42200	SPL9	Vegetative and reproductive phase change	0.42	3.03	8.60E-03	-
AT3G57920	SPL15	Vegetative and reproductive phase change	0.89	0.49	1.34E-02	-
AT1G53160	SPL4	Vegetative to reproductive transition	-1.75	2.89	1.38E-20	+
AT2G25095	miR156a	Vegetative to reproductive transition	0.49	0.32	9.78E-02	-
AT2G33810	SPL3	Vegetative to reproductive transition	-1.55	4.69	4.76E-20	+
AT3G15270	SPL5	Vegetative to reproductive transition	-1.94	1.48	9.23E-15	+
AT4G31877	miR156c	Vegetative to reproductive transition	-0.67	0.51	2.22E-02	-
AT1G17760	Cstf77	Vernalization	0.23	4.42	4.52E-02	-
AT1G71800	Cstf64	Vernalization	0.52	3.29	4.32E-05	-
AT3G18990	VRN1	Vernalization	-0.12	4.78	1.54E-01	-
AT4G00650	FRI	Vernalization	0.26	2.78	1.51E-01	-
AT5G10140	FLC	Vernalization	-6.06	1.29	2.44E-64	+
AT1G61040	VIP5	–	0.42	4.98	3.00E-08	-
AT2G06210	VIP6	–	0.09	5.54	3.63E-01	-
AT2G31650	ATX1	–	0.51	2.96	7.01E-03	-
AT3G48430	REF6	–	0.26	5.21	1.89E-02	-
AT4G20400	Jmj4	–	0.22	5.26	1.81E-02	-
AT5G04240	ELF6	–	0.34	4.96	4.65E-04	-
AT1G08970	NFYC3	–	-0.64	5.32	1.57E-15	-
AT1G14400	UBC1	–	-0.59	6.65	1.10E-10	-
AT1G54830	NFYC9	–	-0.57	4.25	8.50E-08	-
AT1G55250	HUB2	–	-0.12	4.83	2.25E-01	-
AT1G56170	NFYC2	–	-0.29	3.59	2.10E-02	-
AT1G76710	SDG26	–	-0.01	3.53	9.47E-01	-
AT1G77080	MAF1	–	-0.31	5.01	2.71E-04	-
AT1G77300	EFS	–	0.87	5.69	2.31E-11	-
AT1G79730	ELF7	–	0.58	5.26	2.31E-11	-
AT2G02760	UBC2	–	-0.35	6.12	2.08E-05	-
AT2G23380	CLF	–	0.18	4.07	2.68E-01	-
AT2G33835	FES	–	0.18	3.32	1.16E-01	-
AT2G44950	HUB1	–	0.11	4.92	2.45E-01	-
AT2G45640	SAP18	–	-0.86	5.11	1.98E-15	-
AT3G12810	PIE1	–	0.93	5.33	1.07E-17	-
AT3G24440	VIL1	–	0.41	3.99	3.18E-04	-
AT3G33520	ESD1	–	-0.16	4.09	1.60E-01	-

AT3G49600	UBP26	–	0.41	4.92	2.39E-05	-
AT4G15880	ESD4	–	0.00	4.68	9.60E-01	-
AT4G16845	VRN2	–	-0.03	4.17	7.95E-01	-
AT4G29830	VIP3	–	-0.22	3.96	1.23E-02	-
AT4G32980	ATH1	–	0.94	4.91	2.84E-15	-
AT4G39400	BRI1	–	0.22	7.58	1.34E-01	-
AT5G11530	EMF1	–	0.43	4.70	4.55E-04	-
AT5G16320	FRL1	–	0.09	2.57	6.41E-01	-
AT5G23150	HUA2	–	1.38	5.55	2.97E-26	+
AT5G37055	SEF	–	-0.44	2.64	2.11E-03	-
AT5G51230	EMF2	–	0.36	5.12	8.51E-06	-
AT5G61150	VIP4	–	0.07	5.73	4.71E-01	-
AT5G65050	MAF2	–	-0.27	5.31	2.58E-03	-
AT5G65060	MAF3	–	-0.64	3.89	9.91E-09	-
AT5G65070	MAF4	–	-0.20	0.46	4.02E-01	-

Supplementary table 4. Flowering time gene expression.

Change in gene expression of curated genes involved in flowering time in Arabidopsis, as detected using Illumina RNAseq for *vir-1* compared with the VIR-complemented line. In all, 12.2% of flowering time genes show a change in mRNA level expression in the *vir-1* mutant. Source of flowering time genes: George Coupland, Cologne: https://www.mpipz.mpg.de/14637/Arabidopsis_flowering_genes **[Linked to Figure 6].**

1300

Primer name	Primer sequence	Experiment	Gene or gene coordinates
At1g29550 F	ATGGTGGTTACGGATTCTCCA	Chimeric RNA detection RT-PCR	AT1G29550-AT1G29560
At1g29560 R	TTAAACTCCATCTCCCTCTTT		
F_spl2_A	GCTGTGTTCCTTTTCTCAGCA	Splicing events validation RT-PCR	AT2G27385
R_spl2_A	CTGCCTTGGAGTTCTGCTTC		
F_spl5_A	AGGGATAAGCTCTTCTTTTTCC	Splicing events validation RT-PCR	3:12559692–12559814
R_spl5_A	CGACGGTGACAACGAACC		
F_spl7_AB	GTGGTGTTGAGCCGGAGT	Splicing events validation RT-PCR	AT3G42806
R_spl7_B	CTTTCTCGGTGGCTTTTCTC		
F_spl8_B	ATATGGACGATACTTTATACCCTTTG	Splicing events validation RT-PCR	AT3G62040
R_spl8_B	AGCCATGGTGGTTCCATATT		
F_spl9_AB	AATATTTTCCGGTGAATAGCC	Splicing events validation RT-PCR	AT3G26395
R_spl9_B	AAGCCCAGAATCCGGTGA		
CCA1_For	GATGATGTTGAGGCGGATG	RT-qPCR (clock phenotype)	AT2G46830
CCA1_Rev	TGGTGTTAACTGAGCTGTGAAG		
UBC_For	CTGCGACTCAGGGAATCTTCTAA	RT-qPCR (clock phenotype)	AT5G25760
UBC_Rev	TTGTGCCATTGAATTGAACCC		
F_GFP_CDS_T7prom_NotI	GCGGCCGC TAATACGACTCACTATAGGGAGA ATGAGTAAAGGAGAAGAACTTTTCACTG	PCR	mGFP
R_GFP_CDS_AscI	GGCGCGCC TTATTTGTATAGTTCATCCATGCCATG		
FLC-Fwd	GAGCCAAGAAGACCGAACTC	RT-qPCR (flowering phenotype)	AT5G10140
FLC-Rev	TTCTGCTCCCACATGATGA		
RT41clip	NNGTATNNNAGATCGGAAGAGCGTCGTGgatc CTGAACCGC	miCLIP library preparation	–
RT48clip	NNTGTGNNNAGATCGGAAGAGCGTCGTGgatc CTGAACCGC		
RT49clip	NNTTCTNNNAGATCGGAAGAGCGTCGTGgatc CTGAACCGC		
RT50clip	NNTTTCNNNAGATCGGAAGAGCGTCGTGgatc CTGAACCGC		

1301

1302 **Supplementary table 5. Primers used in this study.**

1303

List of Figure Supplements

Supplementary figure 1. Properties of nanopore DRS sequencing data.[Linked to Figure 1].

Supplementary figure 2. 3′ end processing is revealed by nanopore DRS. [Linked to Figure 2].

Supplementary figure 3. Nanopore DRS with cap-dependent ligation of 5′ adapter RNA. [Linked to Figure 3].

Supplementary figure 4. Patterns of splicing revealed using nanopore DRS. [Linked to Figure 4].

Supplementary figure 5. Identification of VIR-dependent m^6A transcriptome-wide. [Linked to Figure 5].

Supplementary figure 6. Changes in the gene expression of circadian clock components and in RNA 3′ end formation in the *vir-1* mutant. [Linked to Figure 6].

Supplementary table 1. Properties of the nanopore DRS sequencing data.[Linked to Figures 1 through 6].

Supplementary table 2. Adapter detection using BLASTN rules approach. [Linked to Figure 3].

Supplementary table 3. Splice junctions supported by nanopore DRS and Illumina RNAseq.[Linked to Figure 4].

Supplementary table 4. Flowering time gene expression. [Linked to Figure 6].

Supplementary table 5. Primers used in this study.